https://doi.org/10.5194/cp-2024-22
Preprint. Discussion started: 21 March 2024

Climate of the Past Discussions

Diagnosing the controls on desert dust emissions through the Phanerozoic

Yixuan Xie[1], Daniel J. Lunt[1], and Paul J. Valdes[1]

[1]School of Geographical Sciences, University of Bristol, Bristol BS8 1SS, UK

Correspondence: Yixuan Xie (yixuan.xie@bristol.ac.uk)

Abstract. Desert dust is a key component of the climate system, as it influences Earth's radiative balance and biogeochemical cycles. It is also influenced by multiple aspects of the climate system, such as surface winds, vegetation cover, and surface moisture. As such, geological records of dust deposition or dust sources are important paleoclimate indicators; for example, dust records can be used to decipher aridity changes over time. However, there are no comprehensive records of global dust variations on tectonic time scales (10's of millions of years). Furthermore, although some modelling studies have focused on particular time periods of Earth's history, there has also been very little modelling work on these long timescales. In this study, we establish for the first time a continuous model-derived timeseries of global dust emissions over the whole Phanerozoic (the last 540 million years). We develop and tune a new offline dust emission model, DUSTY, driven by the climate model HadCM3L. Our results quantitatively reveal substantial fluctuations in dust emissions over the Phanerozoic, with high emissions in the Late Permian to Early Jurassic ($\times$4 pre-industrial levels), and low emissions in the Devonian-Carboniferous ($\times$0.1 pre-industrial levels). We diagnose the relative contributions from the various factors driving dust emissions and identify that the non-vegetated area plays a dominant role in dust emissions. The mechanisms of paleo hydrological variations, specifically the variations in low-precipitation-induced aridity, which primarily control the non-vegetated area, are then diagnosed. Our results show that paleogeography is the ultimate dominating forcing with the dust emissions variations explained by indices reflecting the land-to-sea distance of tropical and subtropical latitudes, whereas CO_2 plays a marginal role. We evaluate our simulations by comparing them with sediment records and find fair agreement. This study contributes a quantified and continuous dust emission reconstruction, as well as an understanding of the mechanisms driving paleohydroclimate and dust changes over Earth's Phanerozoic history.

1 Introduction

Dust plays a pivotal role in the Earth system. Dust affects the climate system in various ways. Dust modulates the Earth's radiation budget directly by scattering, absorbing and re-emitting radiation, but also indirectly regulates the Earth's radiation balance by stimulating cloud and precipitation formation processes (e.g. Schepanski, 2018). In addition, the deposition of dust onto the Earth's surface provides nutrients such as nitrogen, sulfur, iron and phosphorus, which affect the corresponding ecosystems and, ultimately, the global carbon cycle (Mahowald et al., 2017). For example, dust is the dominant external source

https://doi.org/10.5194/cp-2024-22
Preprint. Discussion started: 21 March 2024

Climate of the Past Discussions

of iron to the ocean, and the supply of iron is a limiting factor on marine life in large parts of the ocean and therefore influences the ability of the ocean to regulate atmospheric CO_2 (Jickells et al., 2005).

On the other hand, the climate system regulates dust processes in various ways. Rainfall, evapotranspiration, vegetation and the associated vegetation cover have an effect on sediment availability (Marx et al., 2018). Soil moisture, sediment particle characteristics and surface wind jointly control the dust entrainment (Kok et al., 2012). In addition, shifts in wind regimes, such as the position of synoptic-scale circulation systems, and changes in clouds and precipitation at smaller-scale zones influence the transportation and deposition of dust (Marx et al., 2018).

The estimated global annual dust emission flux is about 2000 Mt, originating from the world's major deserts located in Africa, China and Mongolia, Australia, central and southwest Asia and the United States (Shao, 2001). The majority of the contemporary dust source regions are located in subtropical regions, which are associated with the position of the Hadley circulation: less rainfall is produced in the mid-latitude Hadley Cell descending branch than its tropical ascending branch as a result of the meridional heat and energy transportation (Diaz and Bradley, 2004; Nguyen et al., 2013), and hence lead to the broadly distributed subtropical aridity. In addition, the contribution of dust emissions from high-latitude paraglacial dust source regions is well constrained, accounting for about 5% of the overall dust budget (Bullard et al., 2016).

Because arid areas are in general associated with relatively high dust emissions, geological records of changes in dust emissions in Earth's past serve as a reliable archive for environmental and climate variations in aridity. In addition, past climates provide a natural laboratory for modelling studies which aim to explore controls on dust emissions.

Existing records of past dust emission/deposition show high variability through time. Reconstructions are most abundant in the Quaternary (the last 2.6 million years) and indicate substantial glacial-interglacial variability – the Earth becomes dustier during glacial periods than interglacial periods (e.g. Lamy et al., 2014; Fitzsimmons et al., 2013) and records compiled in (Muhs, 2013) and (Kohfeld and Harrison, 2001). Studies have indicated that the more substantial glacial dust deposits could be attributed to increased wind intensities, a less vigorous hydrological cycle, decreased soil moisture, decreased vegetation cover, and exposed continental shelves (Winckler et al., 2008; Muhs, 2013), all of which are ultimately caused by variations in the Earth's orbital parameters.

Similar orbital-driven dust (or aridity) records are also identified much further back in time, as early as the Late Cretaceous (Niedermeyer et al., 2010; Vallé et al., 2017; Zhang et al., 2019). Moreover, the variability in dust (or aridity) on timescales older than the Quaternary is explained as responses to regional or global cooling (DeCelles et al., 2007; Bosboom et al., 2014; Licht et al., 2016; Zhang et al., 2016), atmospheric CO_2 concentration variations (Wang et al., 2023), tectonic movements (Rea et al., 1998; Licht et al., 2016; Farnsworth et al., 2019; Zhu et al., 2020; Anderson et al., 2020; Yang et al., 2021; Lin et al., 2024), or the absence of land vegetation (Liu et al., 2020). However, these existing records and modelling studies have a relatively small scope, either spatially (only for a specific region) or temporally (only for a specific time period or a couple of time slices) or both, and there is also a lack of geological records of global dust variations through time. As such, our knowledge of the dust (or aridity) distributions, variations and the underlying driving forces in the Earth's deep time still remain insufficiently understood.

https://doi.org/10.5194/cp-2024-22
Preprint. Discussion started: 21 March 2024


Climate of the Past Discussions

The aim of this study is, therefore, to investigate (1) How do the global dust emissions change through the Phanerozoic? (2) What are the causes and mechanisms of these changes? In order to do this, we develop a new offline dust emission model – DUSTY, which is then driven by the output from a set of 109 General Circulation Model (GCM) simulations covering the whole Phanerozoic (last 540 million years).

The DUSTY model and the underlying GCM and GCM simulations are described in section 2. The DUSTY model is tuned to improve its simulations of the modern, described in Section 3. The paleo dust emissions simulations covering the whole Phanerozoic are then carried out with the tuned DUSTY model. Results are shown in section 4, plus analyses of the contributing factors and the driving force of the Phanerozoic dust emissions variations. The credibility of our simulated dust emissions is evaluated with a comparison to geological records, with discussions of the implications and limitations of this study in section 5.

2 Methods

The following section describes the dust emission model "DUSTY" developed for this study, the GCM that is used to drive the DUSTY model, and the simulations that have been carried out with the GCM.

2.1 The dust emission model "DUSTY"

The DUSTY model developed for this study is an offline model. It is designed to be driven by dust-relevant variables from any climatological field, either the output from a GCM or observations, in order to calculate dust emissions for a particular climate scenario. Applying an offline dust model can make the dust simulation more efficient than using a coupled dust scheme within a GCM - allowing multiple sensitivity studies to be carried out without having to run the GCM multiple times. Also, for this study, due to the fact that we are simulating multiple time periods, we focus only on dust emissions rather than transport and deposition, in order to save computational cost. The dust emission model is designed to match the same spatial and temporal resolution of its driving input.

The following dust-relevant fields are used to drive the DUSTY model: the land-sea distribution (l; equal to 0 or 1), the bare soil fraction of the land surface (b; varying from 0 to 1, non-vegetated area hereafter), the soil moisture (m; units ($kg\,m^{-2}$)), the snow cover (s; units ($kg\,m^{-2}$)) and the near-surface (10 meter height) wind velocity (u and v; zonal and meridional respectively, both units ($m\,s^{-1}$)). The spatial resolution of the dust model for this study is 96 × 73 grid points, which is 3.75º × 2.5º in longitude and latitude respectively, corresponding to the driving climate model (see Section 2.2).

The choice of the variables mentioned above is similar to other dust models. Vegetation and snow cover are commonly considered to inhibit dust emission from land surfaces and are generally represented in dust models with empirical global uniformed threshold values, or as a linear function with no threshold (Ginoux et al., 2001; Miller et al., 2006; Kok et al., 2014). The formulation in our dust emission model assigns a linear function and a threshold for both (b_t and s_t respectively), which the value is defined by further tuning process (Equations 3 and 5 below). Soil moisture is widely considered to suppress dust entrainment. Here we represent this with a simplified threshold-based (m_t) linear formulation (Equation 4 below), instead of

https://doi.org/10.5194/cp-2024-22
Preprint. Discussion started: 21 March 2024

Climate of the Past Discussions

considering it as a factor of threshold friction velocity of soil particles as in previous dust schemes (Pérez et al., 2011; Ginoux et al., 2001). As shown by many studies (e.g., Bagnold, 1941; Gillette and Stockton, 1989; Shao et al., 1993), dust emissions can be expressed in terms of surface wind speed above a threshold (U_{t1}), and the dust emission flux is approximately proportional to the third power of the wind speed. Our dust emission model adapts the formulation developed by (Gillette and Passi, 1988), which is also widely used in dust models such as (Tegen and Fung, 1994; Ginoux et al., 2001; Kerkweg et al., 2006; Miller et al., 2006; Chen et al., 2017). We also add a maximum threshold (U_{t2}) for dust emissions to avoid spuriously large emissions when the surface wind speed is extremely strong (Equation 6). There are some factors omitted in this dust emission model compared to some existing dust schemes – the effect of particle size, their soil characteristics and mineralogical features that are believed to be factors for friction velocity of dust entrainment are not included in our dust emission model due to the absence of information on these aspects on the timescales we are addressing here. In addition, 'preferential sources areas'(Zender et al., 2003; Cakmur et al., 2006) which are constrained by the surface topography as 'hydrological basins', are not considered in this dust emission model for the same reasons.

The total dust emissions index, d (no units) of each grid box, is the product of each individually ascribed emission index (Equation 1). d_l, d_b, d_m, d_s, d_U are corresponding emission indices associated solely with the land-sea distribution, the non-vegetated area, the soil moisture, the snow and the near-surface wind, as calculated by Equations 2 to 6 respectively.

$$d = d_l * d_b * d_m * d_s * d_U \tag{1}$$

$$d_l = l \tag{2}$$

$$d_b = \begin{cases} b, & \text{if } b > b_t \\ 0, & \text{otherwise} \end{cases} \tag{3}$$

$$d_m = \begin{cases} (m_t - m)/m_t, & \text{if } m < m_t \\ 0, & \text{otherwise} \end{cases} \tag{4}$$

$$d_s = \begin{cases} (s_t - s)/s_t, & \text{if } s < s_t \\ 0, & \text{otherwise} \end{cases} \tag{5}$$

$$U = \sqrt{u^2 + v^2}, \qquad d_U = \begin{cases} 0, & \text{if } U < U_{t1} \\ (U - U_{t1}) * U^2, & \text{if } U_{t1} \le U \le U_{t2} \\ (U_{t2} - U_{t1}) * U_{t2}^2, & \text{if } U > U_{t2} \end{cases} \tag{6}$$

https://doi.org/10.5194/cp-2024-22
Preprint. Discussion started: 21 March 2024


Climate of the Past Discussions

Specifically, the land-sea distribution gives the basis for subsequent calculations as all the dust emissions are only considered over land areas. The calculation of consequent dust emissions related to bare soil, soil moisture and snow cover are all threshold-based linear relational expressions. The corresponding index for dust emissions induced by surface winds is calculated as a cubic relationship with two thresholds.

$$D = C_2 * d \tag{7}$$

A coefficient C_2 is here used to calibrate the total dust emissions, D (Equation 7), and to convert to units of kg m^2 s^{-1}.

In addition, The dust emission model also produces dust emissions with various combinations of those dust-relevant fields, either included or not included. Using the same naming convention as in equation 7, the emissions calculated are D^l, D^{lb}, D^{lbm}, D^{lbms}, D^{lbU}, D^{lbmU}, D^{lbsU}, as given in equation 8. Similar to C_2, different coefficients (C_1, C_3, C_4, C_5) are used in order to scale the emissions with various process combinations. C_1 is chosen such that the global dust emissions in D^{lbms} are equal to D^{lbmsU}, C_3, C_4, C_5 are chosen such that the global dust emissions in D^{lbU}, D^{lbmU} and D^{lbsU} are equal to D^{lbms}.

$$\begin{aligned}
D^l &= C_1 * d_l \\
D^{lb} &= C_1 * d_l * d_b \\
D^{lbm} &= C_1 * d_l * d_b * d_m \\
D^{lbms} &= C_1 * d_l * d_b * d_m * d_s \\
D^{lbU} &= C_3 * d_l * d_b * d_U \\
D^{lbmU} &= C_4 * d_l * d_b * d_m * d_U \\
D^{lbsU} &= C_5 * d_l * d_b * d_s * d_U
\end{aligned} \tag{8}$$

2.2 The GCM

For this study, the DUSTY model is driven by simulations carried out with a General Circulation Model (GCM) HadCM3BL-MOSES2.1a-TRIFFID (HadCM3BL-M2.1aD in the naming convention of Valdes et al. (2017); henceforth HadCM3L). This is a coupled atmosphere-ocean-vegetation model. The atmospheric component of HadCM3L solves the primitive equation set of White and Bromley (1995) through the Arakawa staggered B-grid scheme from Arakawa and Lamb (1977). Parameterisations include the convection scheme of Gregory et al. (1997), the large-scale precipitation scheme of Wilson (1998), the radiation scheme of Edwards and Slingo (1996), and the clouds scheme of Bushell (1998). The ocean component is based on the model of Cox et al. (1984), which is a three-dimensional ocean model. Parameterisations include the ocean mixed layer schemes of Turner and Kraus (1967). Modifications to the ocean vertical diffusion and isopycnal diffusion due to the model's lower resolution are described in detail in Valdes et al. (2017). There are also modifications in the bathymetry of the North Atlantic, which improves the reality of heat transports in the coupled system and alleviates the need for flux correction and makes the model more appropriate for paleo simulations.

https://doi.org/10.5194/cp-2024-22
Preprint. Discussion started: 21 March 2024

Climate of the Past Discussions

The land surface scheme MOSES2.1 calculates the energy and moisture between the land surface and the atmosphere and updates the relevant surface and subsurface variables (Cox et al., 1999). It is coupled with an interactive vegetation model, TRIFFID, via nine land cover types: broadleaf trees, needleleaf trees, shrubs, C3 grasses, C4 grasses, urban, inland water, bare soil and land ice. TRIFFID takes the averaged flux of carbon from MOSES2.1, calculates the growth and expansion of five defined plant functional types and updates the vegetation fractions and parameters through competitive, hierarchical formulation.

HadCM3L has a horizontal resolution of 96 × 73 grid points in both the atmosphere and the ocean, which is 3.75º × 2.5º in longitude and latitude, and 19 hybrid vertical levels in the atmosphere and 20 vertical levels in the ocean with finer definition closer to the surface. It is of relatively lower resolution compared to recent state-of-the-art CMIP6 models, therefore, it is particularly computationally efficient and applicable for multi-million-year scale simulations. The model has been used widely in pre-Quaternary climate modelling studies (e.g. Marzocchi et al., 2015; Wade et al., 2019; Jones et al., 2022).

Since Valdes et al. (2017), the model has undergone several improvements, the most significant of these is a tuning process designed in particular to improve the deep-time climate simulations. The changes made follow those described in Sagoo et al. (2013); Kiehl and Shields (2013), primarily targetting parameters associated with clouds; this results in a flatter meridional temperature gradient in warm climates, which is in better agreement with paleoclimate proxies. More details of this process are described in Ross (2023).

2.3 The GCM simulations

This study uses 3 series of 109 experiments each, S_1, S_{1noCO2} and S_2, all carried out with HadCM3L, corresponding to roughly 109 geological stages covering the whole Phanerozoic (since 541 million years). Similar simulations are described in Valdes et al. (2021). However, the Valdes et al. (2021) simulations do not include the tuning processes described in section 2.2. Series S_2 does include those tuning, but is otherwise identical to series S_1. The boundary conditions to drive the S_1 and S_2 simulations include (1) solar constant following (Gough, 1981); (2) atmospheric CO_2 concentrations following (Foster et al., 2017); and (3) paleogeography (the configuration and height/depth of the continents and oceans) following (Scotese and Wright, 2018). The boundary conditions used to drive S_{1noCO2} are identical, but with a fixed atmospheric CO_2 concentration at 276.01 ppm. These simulations have been run for an additional 3000 years beyond those described in (Valdes et al., 2021). To conduct this dust study, each of the 109 experiments is also run for an additional 30 years with the dust-relevant variables (m, s, u, v) output at an hourly resolution.

The "0 Ma simulation" (the latest of the 109 simulations, corresponding to the pre-industrial configuration) is designed to be consistent with the rest of the paleo simulations in terms of most of the boundary conditions, for example, having homogeneous soil properties. As such, it is not the most accurate possible simulation of the pre-industrial climate. In order to tune the dust model with the pre-industrial scenario, we therefore also carry out another "standard pre-industrial simulation" with HadCM3L, which has more realistic pre-industrial boundary conditions. The main differences between them are – (1) the vegetation in the standard pre-industrial simulation is from observations, whereas the vegetation in the 0 Ma simulation is calculated by the coupled vegetation scheme; (2) the topography of the standard pre-industrial simulation is from observation,

https://doi.org/10.5194/cp-2024-22
Preprint. Discussion started: 21 March 2024

whereas the topography of the 0 Ma simulation is from the (Scotese, 2016) reconstructions; (3) the surface variables, primarily soil properties, are globally homogeneous in the 0 Ma simulation but are spatially varied based on observations in the standard pre-industrial simulation.

3 Dust model tuning

Given that there are uncertainties in the "correct" values of the thresholds b_t, m_t, s_t, U_{t1}, U_{t2} and the coefficients C_1, C_2 etc., it is necessary to design a tuning process to identify the values that give the most realistic results for D. The assumption is that the tuning is carried out for the pre-industrial simulation, and the same tuned variables are assumed to be appropriate for all the paleo simulations.

3.1 Methods of tuning

In order to calibrate the dust model, a target needs to be selected as a benchmark. Theoretically, the target that the model is tuned to should be based on observations. In practice, the parameters commonly provided by modern dust observations are Dust Optical Depth or Aerosol Optical Depth (e.g. Gkikas et al., 2021), which are properties primarily influenced by the suspended dust particles in the atmosphere, whereas our dust model only predicts the surface emissions. Therefore, we use simulated modern dust emissions from other (more complex) coupled climate-dust models as the tuning target. Here we use the multi-model mean of 15 CMIP6 AMIP models (hereafter 15_MMM, Figure 1a) which is the dust emission over the period 2005-2014. In the absence of dust emissions from observations, this is justified partly by the complexity and resolution of CMIP6 models being higher than HadCM3L, which are therefore expected to predict more accurate dust emissions than the dust model in this study; and partly because the mean of several models in general has a lower bias than the output of a single model, and therefore represents a valid tuning target. The global average dust emission rate given by the 15_MMM is $1.96 * 10^{-10}\ kg\, m^{-2} s^{-1}$, which is used to calculate the C_1 in equation (7) in each tuning experiment, so that the standard pre-industrial dust simulation has an identical global mean dust emission rate as the target.

In addition to scaling the global average dust emission rate to the target, the main aim of the model tuning process is to find the optimum choices of the threshold values of the dust model that give the best fit to the spatial pattern of the target. When evaluating the model, it is necessary to use a cost function to quantitatively measure the difference between the simulations and the target. The metric chosen here is the “Arcsin Mielke” score (AMS, Watterson et al. (2014)). For a modelled dust field D, and an observed dust field T, the AMS is defined as

$$AMS = \frac{2000}{\pi} arcsin[1 - mse/(V_D + V_T + (G_D - G_T)^2)] \tag{9}$$

where mse is the mean-square error between T and D, V_D and V_T are the spatial variances of D and T respectively, G_D and G_T are the spatial means of D and T respectively. The AMS has a maximum possible value of 1,000, where the modelled result is identical to the target.

https://doi.org/10.5194/cp-2024-22
Preprint. Discussion started: 21 March 2024

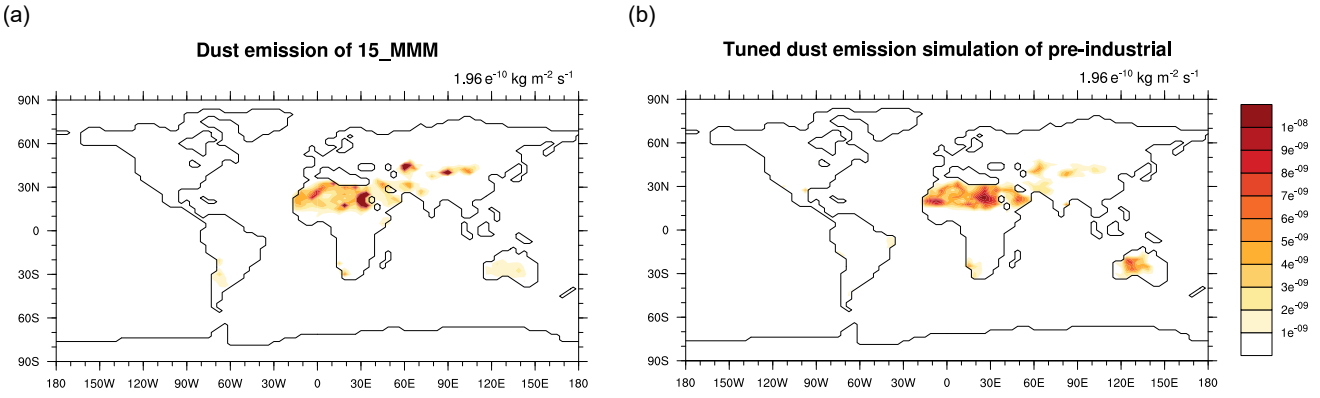

Figure 1. The pre-industrial dust emissions fields **(a)** averaged from the 15 CMIP6 AMIP models, which is used in this study as the tuning target, **(b)** simulated from the tuned DUSTY model. Both values at the top-right are the global mean dust emission rates.

To perform the tuning, a Latin Hypercube Sampling (LHS, Mckay et al. (1979)) method is used. LHS is a stratified-random procedure which provides an efficient way of sampling variables. In this study, the number of samples, which is also the number of tested model versions, is 200. This decision is a trade-off between having as many samples as possible and the cost of computing time. The five-dimensional parameter space where the 200 samples are taken from, is constrained by the range of b_t, m_t, s_t, U_{t1} and U_{t2}. We take a two-step approach here. Firstly, the initial range for each threshold is derived from the variable's distribution in the standard pre-industrial GCM simulation, or based on previous studies. Specifically, the bare soil values of the preindustrial simulations vary from 0 to 1, so the initial test range is set to be the [0.0-1.0]. The soil moisture at the southern edge of the Sahara area, where modern dust emissions are relatively low, is around 20.0 to 24.0 ($kg\ m^{-2}$), so the initial test range is set at a slightly wider range of 18 to 28 ($kg\ m^{-2}$). For snow cover, (Lunt and Valdes, 2002) apply a snow cover threshold in their dust model of 20.0 $kg\ m^{-2}$; as such the initial test range of 15.0 to 25.0 ($kg\ m^{-2}$) is chosen to encompass that value. The global minimum wind speed is around 0.8 $m\ s^{-1}$ and the maximum wind speed over land does not exceed 6.0 $m\ s^{-1}$, as such, a reasonable initial test range of U_{t1} is set as 0.8 to 4.0 ($m\ s^{-1}$), and 4.0 to 6.0 ($m\ s^{-1}$) for U_{t2}. Secondly, starting from the initial test ranges described above, further adjusting (expanding, shrinking or shifting) to the test range has been carried out in an iterative process, with the aim of identifying appropriate ranges for the 200 sampled experiments. The final ranges applied are 0.2 to 0.34 for bare soil, 16.0 to 30.0 ($kg\ m^{-2}$) for soil moisture, 14.0 to 50.0 ($kg\ m^{-2}$) for snow cover, 0.2 to 2.0 ($m\ s^{-1}$) for U_{t1} and 2.0 to 5.5 ($m\ s^{-1}$) for U_{t2}, as shown in Figure 2.

3.2 Tuning results

The results of the tuning exercise are shown in Figure 2. As a post hoc justification of the parameter ranges identified in Section 3.1, the results of the tuning show that the relatively high AMS values (i.e. the best fitting parameters) are not situated close to the edges of the ranges.

https://doi.org/10.5194/cp-2024-22
Preprint. Discussion started: 21 March 2024

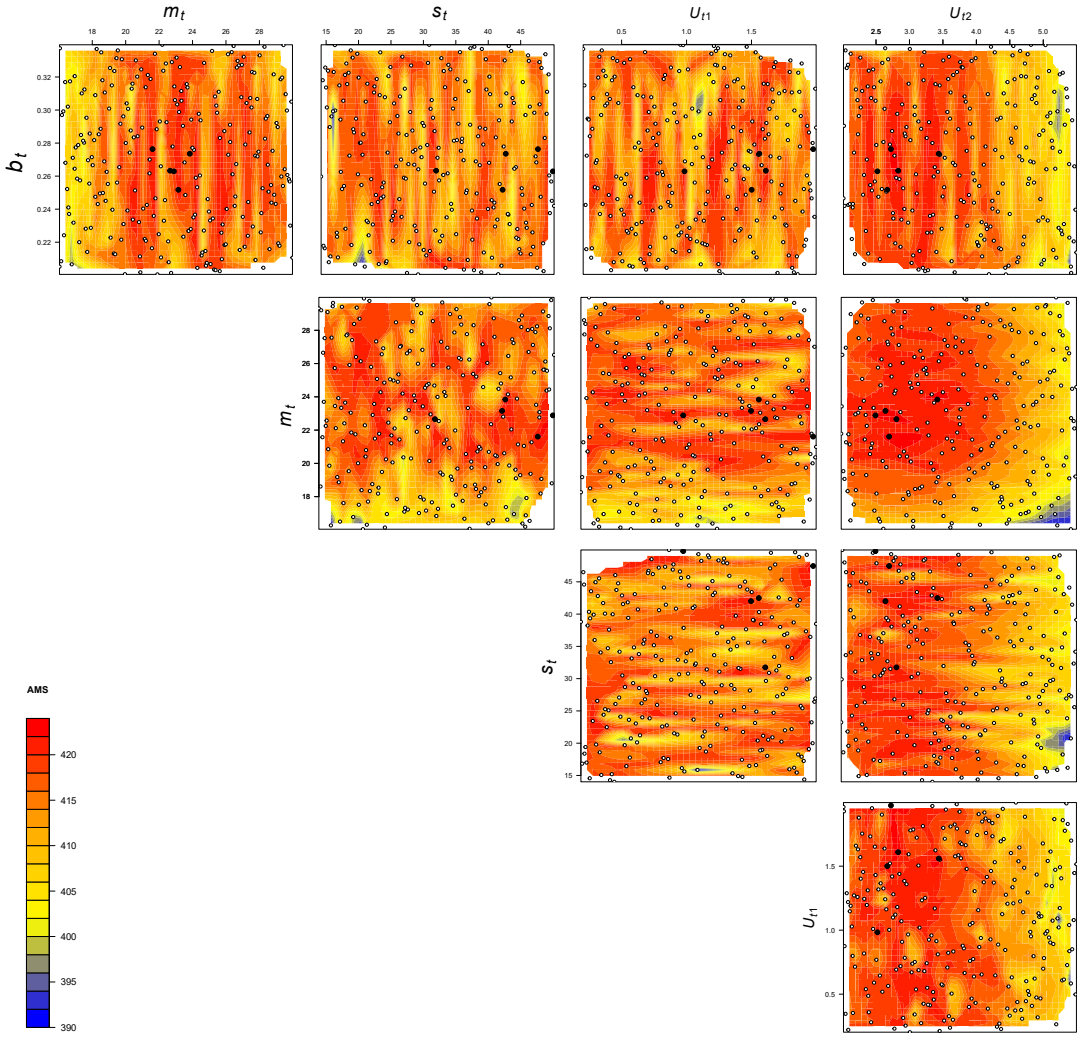

Figure 2. The performance of 200 dust emission model versions with different thresholds, measured by their AMS, compared to the tuning target. The ranges for each threshold shown in this figure are all final ranges, Each panel has 200 dots representing all the samples taken within the corresponding ranges, where the five solid dots are the top-ranked ones.

https://doi.org/10.5194/cp-2024-22
Preprint. Discussion started: 21 March 2024

Climate of the Past Discussions

We select the dust emission model versions with the top five AMS results from the tuning exercise (as shown in black dots in Figure 2). The corresponding thresholds and coefficients are listed in Table 1. The tuned standard pre-industrial dust emission simulation (simulated from tuned parameter set version 1, all maps shown hereafter are results from model version 1 as a representative) is shown in Figure 1b. The tuned simulation generally captures the spatial pattern of global dust emission regions as defined by the 15_MMM, with northern Africa and central Australia predominating, followed by central Asia, and minor regions in South Africa.

Table 1. Summary of thresholds valued applied in the top five DUSTY model versions

Tuned DUSTY model version number	C_1	b_t	m_t	s_t	U_{t1}	U_{t2}
1	1.88e-08	0.26	22.66	31.75	1.61	2.83
2	2.11e-08	0.28	21.61	47.45	1.97	2.72
3	1.69e-08	0.27	23.84	42.49	1.56	3.44
4	1.78e-08	0.25	23.16	42.00	1.50	2.67
5	1.83e-08	0.26	22.88	49.76	0.98	2.52

4 Phanerozoic dust emissions and controls

This section presents the paleo application of the dust model, including the simulated dust emissions over the Phanerozoic (Section 4.1), analysis of the contributions from the factors (Section 4.2), and the evolution of aridity in response to paleogeography (Section 4.3).

4.1 Dust emissions over the Phanerozoic

The five tuned versions of the dust emission model in section 3.2 are applied to all 109 time slices through the Phanerozoic (since 540 Ma). Here we show the simulated global averaged dust emission rate time series in Figure 3, and the simulated dust emission fields for five example time slices (0 Ma, 196Ma, 252Ma, 370Ma, and 530 Ma) in Figure 4 (the dust emission field for all 109 experiments can be found in Appendix in Figure A2-A5). Most notably, the dust emissions are significantly high during the period over the late Permian to the early Jurassic (263 Ma to 191 Ma), where there are two peaks, one covering the Permian-Triassic transition (252 Ma) at the emission rate of $9.1 * 10^{-10}\ kg\ m^{-2} s^{-1}$ and the other spanning the middle Triassic to the early Jurassic (196 Ma) at the emission rate of $8.5 * 10^{-10}\ kg\ m^{-2} s^{-1}$. The emission rates for both peaks are more than four times the pre-industrial level ($1.96 * 10^{-10}\ kg\ m^{-2} s^{-1}$). The dust provenance areas for both peaks are concentrated in the central supercontinent, covering the mid-latitudes, subtropics, and the tropics, as illustrated in Figure 4bc. The global dust emission rate reaches its lowest in the Devonian-Carboniferous transition (366 Ma) at the level of $1.9 * 10^{-11}\ kg\ m^{-2} s^{-1}$, which is almost ten times less than the pre-industrial level. Dust provenance areas are scattered throughout the mid-latitudes in both hemispheres (Figure 4d) at that time. In the early Cambrian (541 Ma to 535 Ma), the oldest simulation we carry out,

https://doi.org/10.5194/cp-2024-22
Preprint. Discussion started: 21 March 2024

Climate of the Past Discussions
Open Access
EGU

dust emission rates ($1.6 * 10^{-10}\ kg\ m^{-2} s^{-1}$) are close to the pre-industrial level, and the dust source regions are centred in the mid-latitudes of both hemispheres (Figure 4e). Evaluations on the simulated dust emission in comparison to geological records will be discussed in section 5.1.

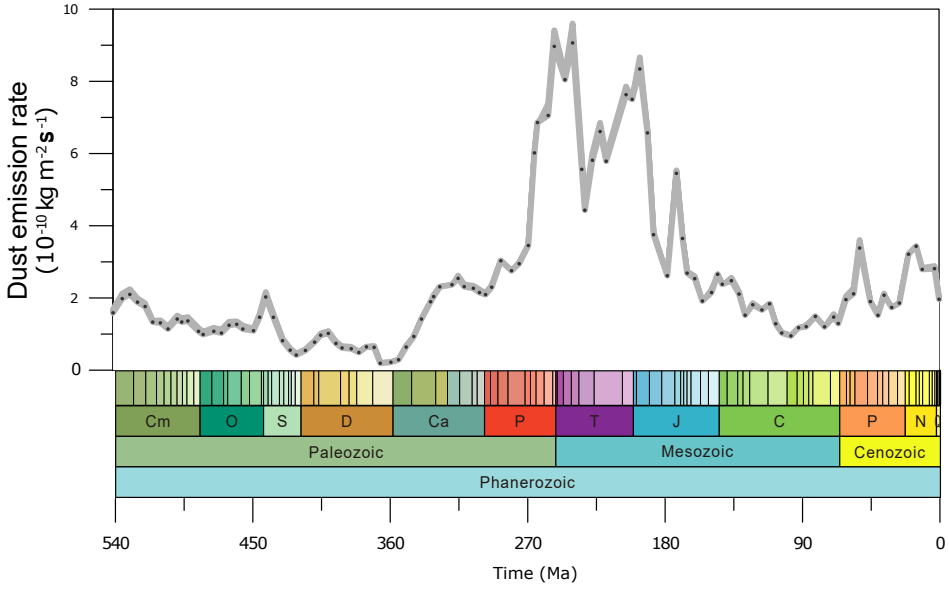

Figure 3. Time series of the simulated global average dust emission rate over the Phanerozoic. The grey shading (not a curve) in the figure is a stack of the results from those five top-ranked model versions, and the dots on it represent the results of model version one to hint at the time intervals between simulations of different time slices.

https://doi.org/10.5194/cp-2024-22
Preprint. Discussion started: 21 March 2024

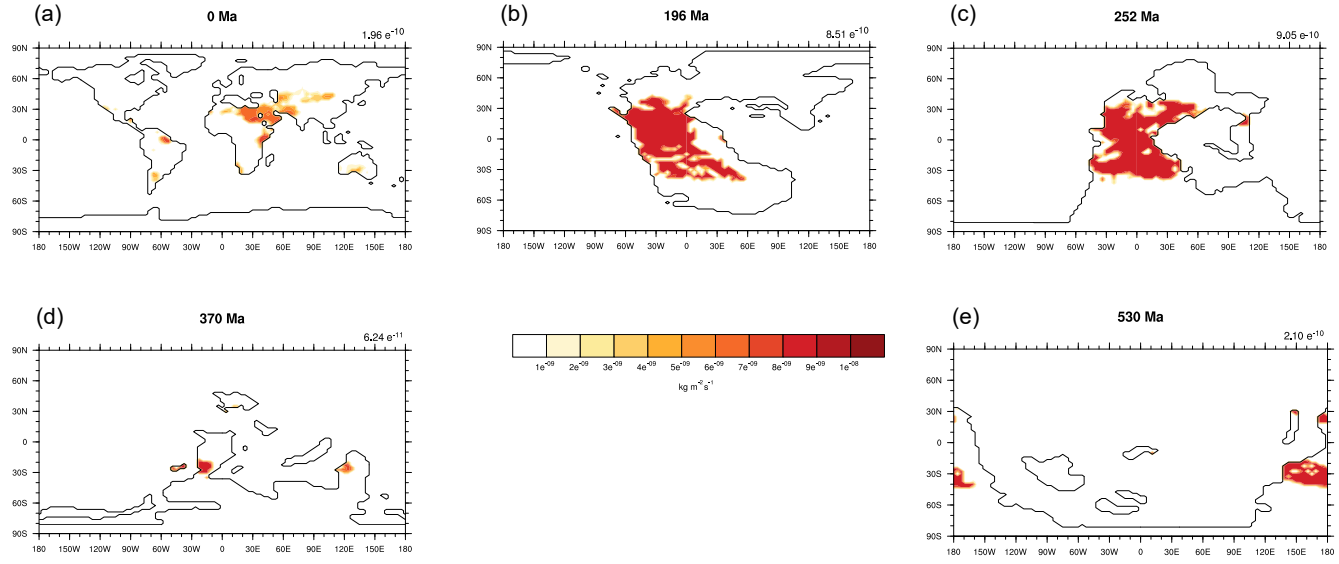

Figure 4. A few examples of the simulated dust emissions. The examples are for **(a)** present day (0 Ma), **(b)** the early Jurassic (196 Ma), **(c)** the early Triassic (252 Ma), **(d)** the late Devonian (370 Ma), and **(e)** the early Cambrian (530 Ma). Values at the top-right of each panel are the corresponding global mean dust emission rate. All unites are $kg\ m^{-2}s^{-1}$.

4.2 Contributing factors to the dust emissions

The simulated dust emissions described in section 4.1 show substantial fluctuations over the Phanerozoic. In order to understand the causes of the fluctuations, we here use a factorisation approach to analyze and quantify the relative importance of each variable (the land-sea distribution l, the non-vegetated area b, the soil moisture m, the snow cover s and the near-surface wind U, all introduced in section 2.1) that is used to drive the dust emission model.

The factorisation is carried out in a two-step approach, where the analysis of l and b is performed as a linear factorisation, whereas the analysis of m, s and U is performed based on the 'linear sum' factorisation method according to (Lunt et al., 2021), which is suitable for diagnosing a multi-variate system. We understand the whole system from a starting point in which there are no dust emissions anywhere on the globe, D^0. We then add the factors l and b sequentially, to produce D^l and D^{lb} respectively (the linear factorisation). We then carry out an unordered addition of the three remaining factors m, s, and U, producing D^{lbm}, D^{lbs}, D^{lbU}, D^{lbms}, D^{lbmU}, D^{lbsU} and D^{lbmsU} (see Section 2.1 for the naming convention). Details of the factorisation are described in the appendix with the factorisation concept illustrated in Figure A1. The contributions of each factor are quantified for the land-sea distribution, vegetation, soil moisture, snow cover, and wind, as ΔD^l for the land sea distribution, ΔD^b,ΔD^m,ΔD^s, and ΔD^U, respectively.

The factorisation is applied to all the time slices to quantify the contribution of each factor and how this varies over time, as illustrated in Figure 5. The contribution from the land-sea distribution factor ($\Delta D^l = D^l$, brown line in Figure 5a) results in

https://doi.org/10.5194/cp-2024-22
Preprint. Discussion started: 21 March 2024


Climate of the Past Discussions

dust emissions of about 3.5 kg/m^2 over the early Phanerozoic, increasing to a maximum around 250 Ma, and then decreasing to about 90 Ma before increasing slightly to the modern. Following is the contribution from the non-vegetated area factor (ΔD^b), which reduces the dust emissions remarkably over time. Regarding the reality that non-vegetated area and land-sea distributions are inalienable, the joint contribution from both l and b (ΔD^{lb}) gives a more concrete reflection, which is three times the all-forcing dust emissions (D^{lbmsU}). The addition of m and s both reduce the dust emission. The contribution from m (ΔD^m) is approximately double the all-forcing dust emissions, whereas the contribution from s (ΔD^s) is only 1% of the all-forcing dust emissions. The addition of U alters dust emissions most positively over time but also has adverse effects for a few time periods in the mid-Permian, early-Cretaceous and late-Paleogene. It contributes an average of 44% of the all-forcing dust emissions before the Carboniferous and 27% of the all-forcing dust emissions during the late Permian to the early Jurassic.

The analysis above quantifies the magnitude of each factor to the total global dust emissions for each time slice individually. A complementary approach is to quantify the impact of each factor on the temporal variability of emissions throughout time, i.e., the extent to which the shape of the emission timeseries improves towards the all-forcing emission timeseries as the result of the inclusion of a specific variable. In order to evaluate this, for each combination of factors, we calculate the correlation coefficient of the resulting emissions timeseries with the all-forcing emissions timeseries. We then drive the contribution from the difference in these correlation coefficients, The greatest contribution to the temporal variability in emissions is made by l (66.53%), followed by b (31.86%), U (1.22%), m (0.34%), and finally s (0.05%).

https://doi.org/10.5194/cp-2024-22
Preprint. Discussion started: 21 March 2024

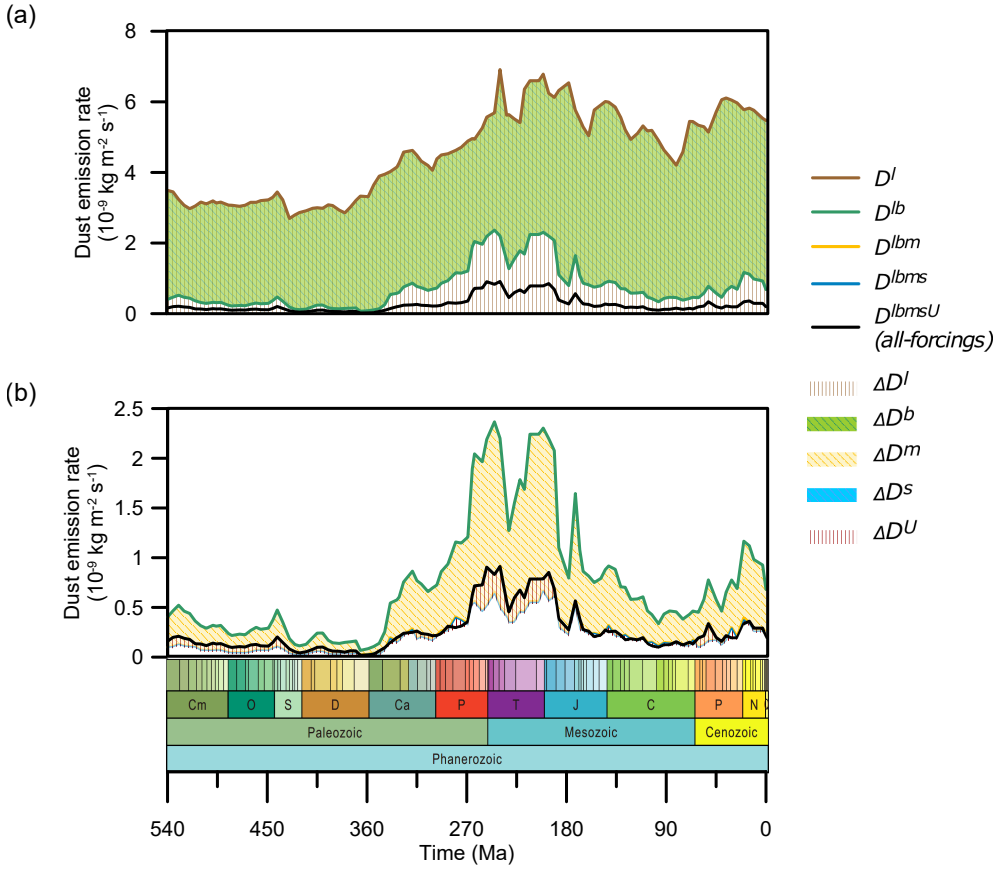

Figure 5. The decomposed contribution of individual factors to the total dust emissions over the Phanerozoic. **(a)** Results for l and b,**(b)** Results for m, s and U. Note that the ranges of y-axes differ between panel **(a)** and **(b)**. All curves refer to the joint dust emissions derived from the corresponding superscript variables, and the shadings refer to the dust emissions contributed from each specific superscript variable. (e.g. D^{lb} refers to the simulated dust emissions when only variables l and b are included in the DUSTY model, and ΔD^{m} refers to the quantified dust emissions contribution of the sole variable m)

4.3 The paleogeographical control on the desert area

As shown in Section 4.2, the combined land and non-vegetated area factors (D^{lb}) dominate the dust emission variations on geological timescales. Given that the non-vegetated area changes implicitly also include the land area changes (i.e. D^{b}=D^{lb}), here we focus on the mechanisms for the changes in non-vegetated areas.

We here measure the extent of aridity with an aridity index (AI) that is threshold-based and inversely proportional to the amount of precipitation:

$$AI = (t_{arid} - precipitation)/t_{arid}), \tag{10}$$

https://doi.org/10.5194/cp-2024-22
Preprint. Discussion started: 21 March 2024

Climate of the Past Discussions
Open Access
EGU

where t_{arid} is set as 0.8 mm/day.

The non-vegetated fraction in the simulations are very closely controlled by the precipitation rate. In particular, the area of precipitation that is less than 0.8 mm/day (represented by the Aridity Index) shows a very strong positive linear relationship with the non-vegetated area (Figure 7ab, correlation coefficient = 0.98). And as we have shown above, the non-vegetated fraction controls the total dust emissions. In addition to the global means, the zonal mean distribution of continental precipitation varies over time (Figure 8c), as does the zonal mean Aridity Index (Figure 8d. The aridity index shows a very similar pattern to the dust emissions (Figure 8e). As such, the continental distribution, combined with the zonal mean precipitation (Figure 8ab) are sufficient to closely approximate the dust emissions (Figure 8e).

The challenge then becomes to understand the controls on zonal mean precipitation (Figure 8a). There are three boundary conditions that are changing over time which must ultimately control the precipitation changes; namely, CO_2, solar constant, and paleogeography. Firstly, in order to explore the impact of CO_2 change, here we take the results from an additional series of GCM simulations, as a sensitivity test. Comparison of results from the S_1 and S_{1noCO2} simulations (described in section 2.3) reveal the negligible effect of CO_2 concentration on the precipitation variation over time (Figure 6b), and therefore aridity (Figure 6a). Hence, we conclude that on these timescales, CO_2 is not a strong control of the aridity. Furthermore, the change in solar constant through the Phanerozoic is linear, whereas the dust emissions change is highly non-linear. As such, we can attribute the mechanism of changes in precipitation, aridity, and ultimately dust emissions, to the only remaining boundary condition change, namely paleogeography.

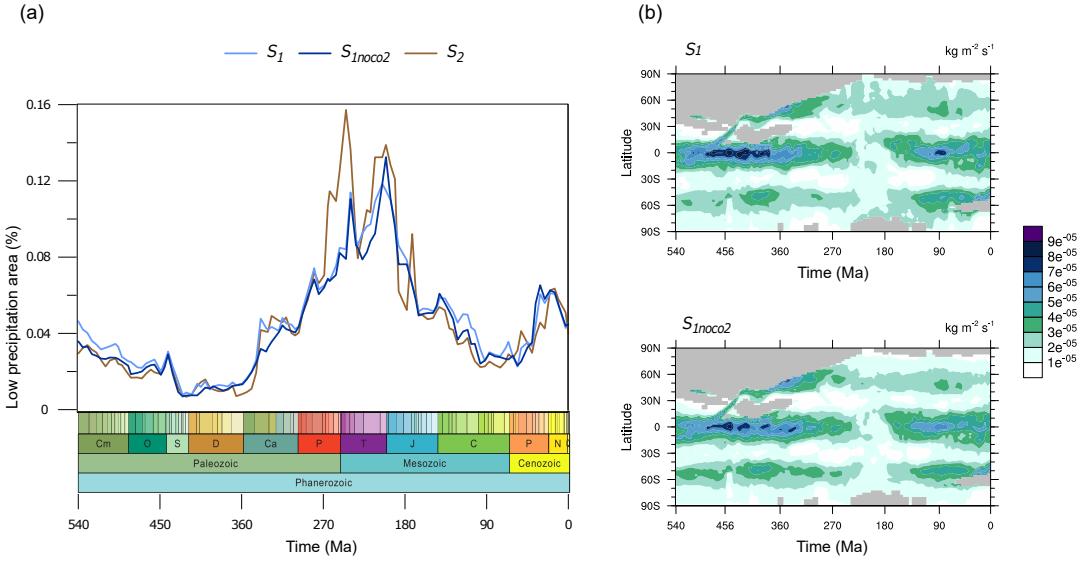

Figure 6. (a) Comparison of low precipitation area fraction time series from three different experimental series: S_1, $S_1 noco2$ and S_2. A daily mean precipitation of less than 0.8 mm is considered low precipitation. **(b)** Comparison of zonal mean land precipitation over the Phanerozoic between experimental series S_1 and $S_1 noco2$.

https://doi.org/10.5194/cp-2024-22
Preprint. Discussion started: 21 March 2024

In general, it may be expected that regions in the continental interiors are more arid due to being remote to oceanic moisture sources. Here we develop indices measuring the distance of the shortest pathway from land to ocean. The distance indices are calculated in the tropical zone (23.5°N to 23.5°S, TD), the subtropical zones in the Northern Hemisphere (35°N to 23.5°N,$NSTD$) and the subtropical zones in the Southern Hemisphere (23.5 °S to 35°S, $SSTD$) respectively, as shown in Figure 7c. During the period prior to the Carboniferous, the global aridity (Figure 7b) shows a remarkably similar temporal evolution to TD and $SSTD$, which drop remarkably in the Silurian and Devonian. Since the Carboniferous, more continents shift to the tropics and the Northern Hemisphere, and the overall growth of global aridity is therefore driven by the combined effect of TD and $NSTD$ until the late Permian (excepting a short drop-down at the late Carboniferous when the $SSTD$ exerts a control). The extreme aridity from the late Permian to the late Triassic is controlled by all three land-sea distance indices, which is due to the fact that the supercontinent covers almost all latitudes during the corresponding times. The extreme aridity can be divided into two peaks during this period. The first aridity extreme at the Permian-Triassic boundary is mainly driven by the $SSTD$, the second aridity extreme at the late Triassic is mainly driven by the TD, while the $NSTD$ contributes equally to both. The land-sea distance indices have decreased in all three latitude zones since the early Jurassic due to continuous continent convergence, resulting in overall humidification until the Cretaceous-Paleocene boundary, where the decrease of $SSTD$ plays a relatively significant role. From the Cenozoic onward, the continents have shifted further northward, resulting in the $NSTD$ being the dominant control of the expanding aridity. Overall, these distance indices are able to approximately explain the change in global mean aridity over time.

As the fundamental driving factor, paleogeography controls the geological timescale aridity and, thus, dessert area variations over the Phanerozoic. The dust source area is consistently found in subtropical land areas of either hemisphere over time, resulting from a relatively constant meridional atmospheric circulation pattern throughout the Phanerozoic. Under this fairly fixed meridional precipitation pattern, it is the drifting and converging of continental land that truly determines the location of desert regions and the amount of dust emissions.

https://doi.org/10.5194/cp-2024-22
Preprint. Discussion started: 21 March 2024

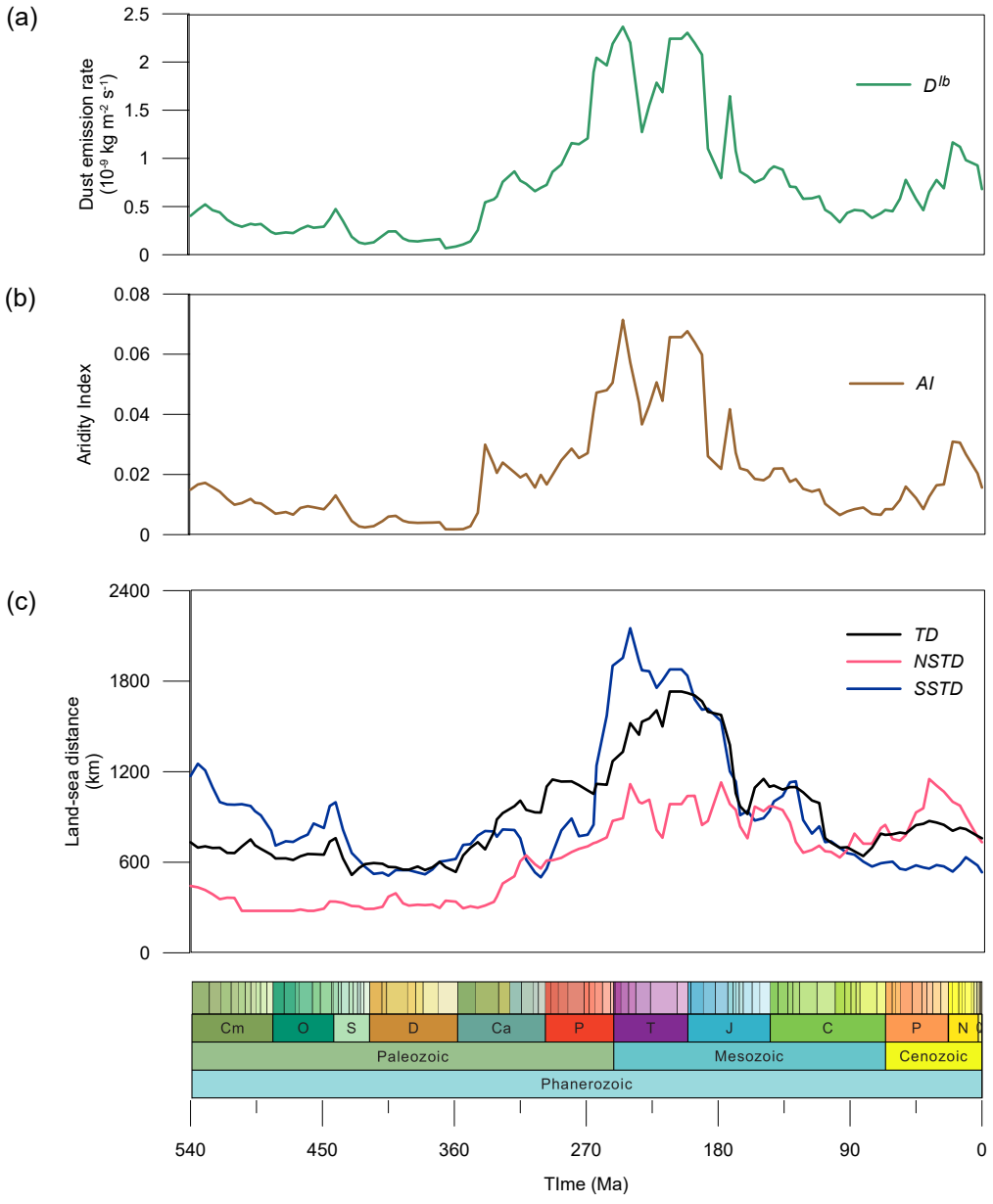

Figure 7. Time series of **(a)** D^{lb}, which is the simulated global average dust emissions jointly contributed from l and b, **(b)** the AI (aridity index), which reflects the lowness of precipitation, and **(c)** the land-sea distance indices, in which TD refers to the tropics, $NSTD$ and $SSTD$ corresponds to the subtropics of the Northern and Southern Hemispheres, respectively.

https://doi.org/10.5194/cp-2024-22
Preprint. Discussion started: 21 March 2024

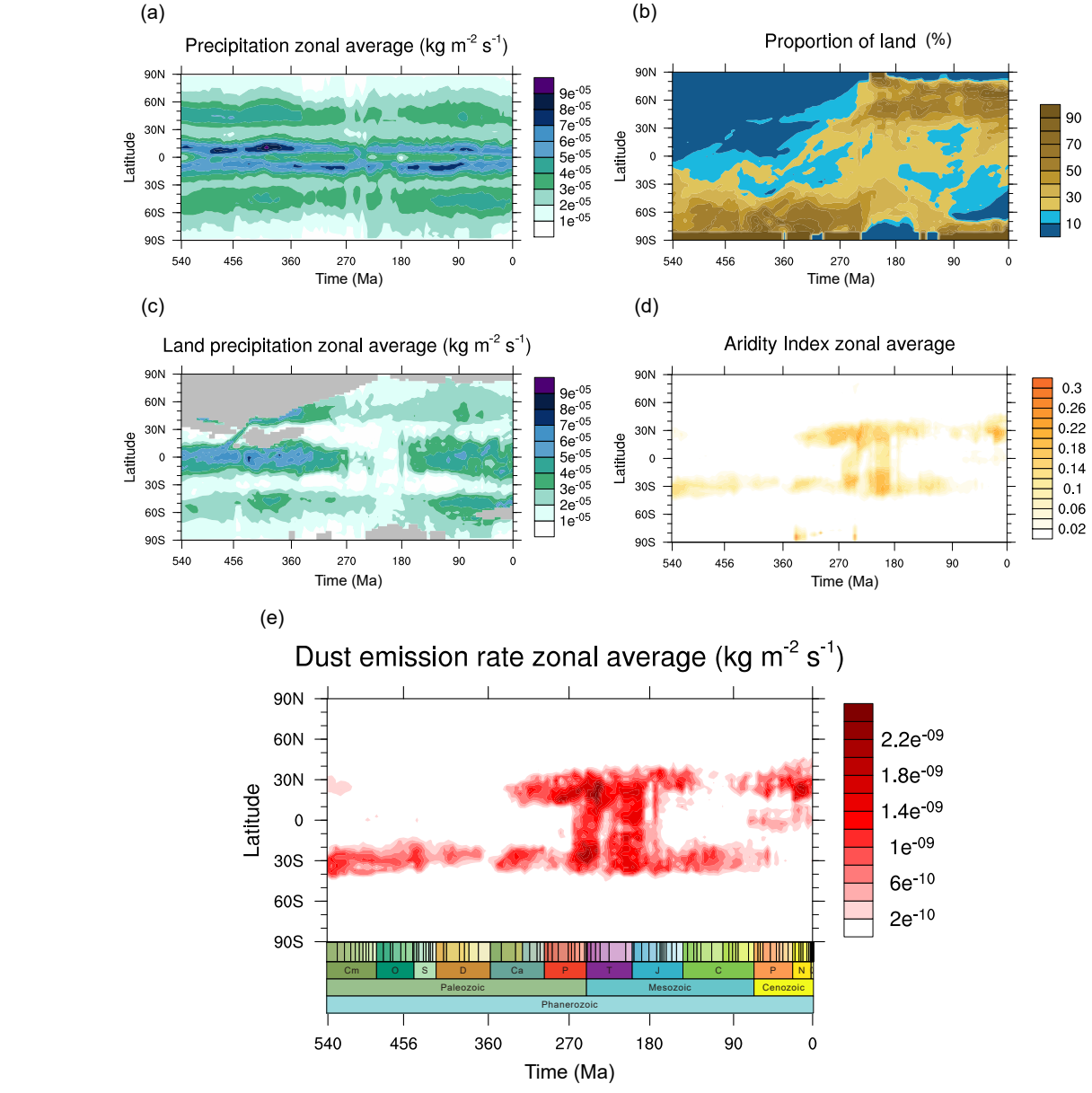

Figure 8. The zonal means of **(a)** the simulated precipitation, **(b)** the proportion of land , **(c)** the simulated precipitation over land, **(d)** the aridity index, **(e)** the simulated dust emissions over the Phanerozoic.

5 Discussion

5.1 Credibility of the simulated Phanerozoic dust

We herein compare evidence from both sediments and modelling to evaluate the simulated Phanerozoic dust emissions.

https://doi.org/10.5194/cp-2024-22
Preprint. Discussion started: 21 March 2024


Climate of the Past Discussions

The evaporite sediment indicators compilation from (Boucot et al., 2013), although not direct evidence of dust emissions, is used here to assess our simulations because evaporites are indicators of arid regions due to its formation mechanism, and also the compilation gives continuous records covering the whole Phanerozoic. How well the model matches with data is evaluated by how well the evaporite data in the compilation agree with estimates of potential evaporite distribution derived from the HadCM3L simulations. There is uncertainty underlying this model-data comparison coming from the algorithm used for predicting evaporites from temperature and precipitation that cannot be quantified within this study.

Notably, the modelled simulated widespread tropical drought – leading to widely distributed potential evaporites – during the late Permian to the early Jurassic (Figure 9ab) coordinates well with the geological sedimentary evidence. Quantitatively, the model performance varies over time, with an average of 35.3% of the evaporite data points predicted correctly by the HadCM3L model. To put this agreement in content, we also derive a "zero skill model", in which the fixed evaporite simulations for 0 Ma are applied for all the paleo timeslices. The zero-skill model gives an average of 4.6% agreement, which is notably lower than what HadCM3L got, suggesting the fair good performance of the model used here in this study (Figure 9e).

https://doi.org/10.5194/cp-2024-22
Preprint. Discussion started: 21 March 2024

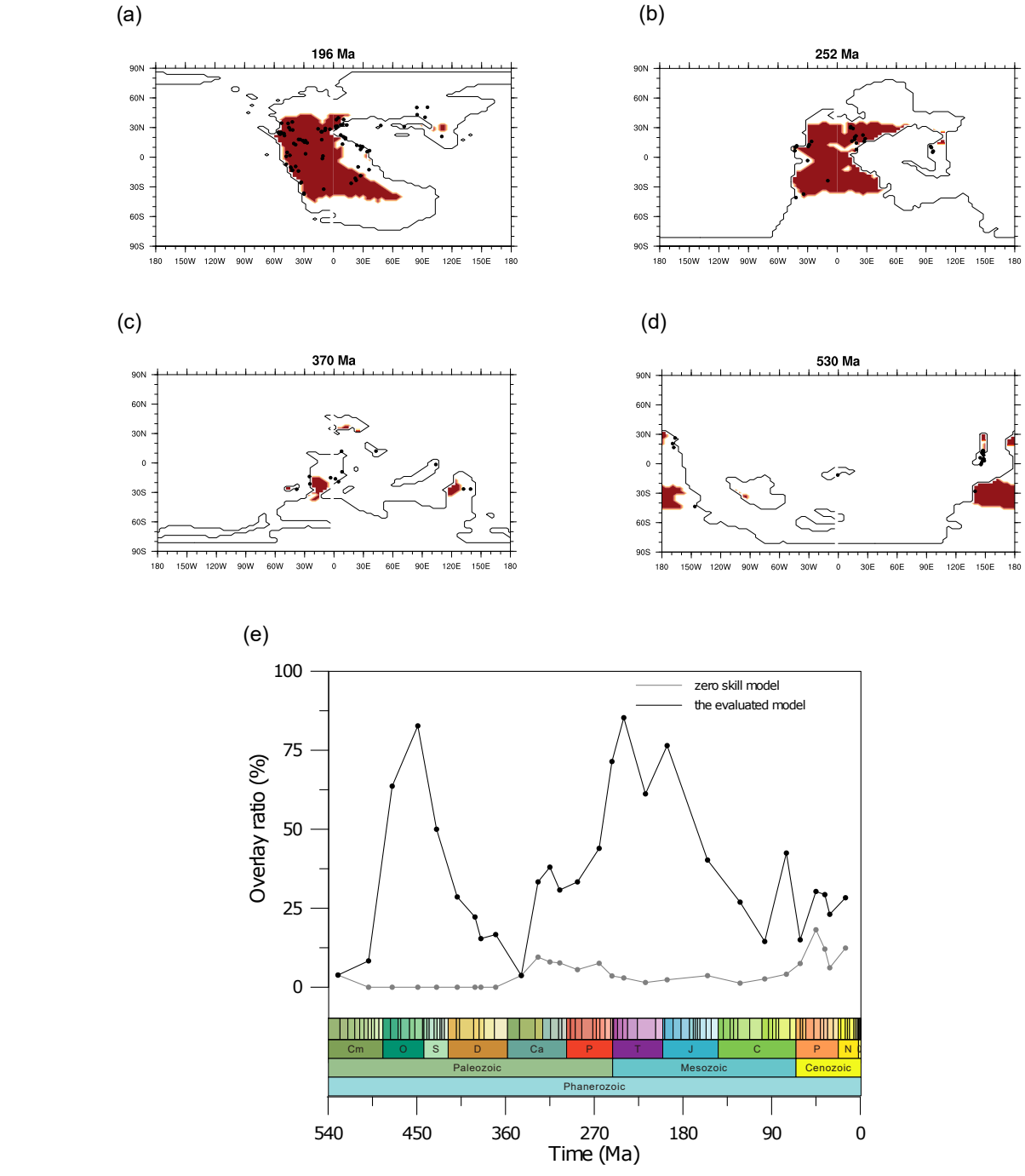

Figure 9. Comparisons of evaporite sedimentary records (dark dots, data from (Boucot et al., 2013)) to the simulated evaporite (area in red) of a few example time slices: **(a)** the early Jurassic (196 Ma), **(b)** the early Triassic (252 Ma), **(c)** the late Devonian (370 Ma), **(d)** the early Cambrian (530 Ma), and **(e)** a time series representing the performance of the model derived by assessing the overlap between model and data over time.

https://doi.org/10.5194/cp-2024-22
Preprint. Discussion started: 21 March 2024


Climate of the Past Discussions

Here, we further focus on the Mesozoic to Cenozoic Asian dessert dust and the Mesozoic Pangean dessert dust to evaluate the accuracy of our simulations.

Our results show that the Asian dessert dust generated since the middle Jurassic (168 Ma), reached a maximum at the Late Jurassic–Early Cretaceous (145 Ma). During the early Cretaceous (131 - 97 Ma), the Asian continent passed through a period without obvious desert dust. The dust provenance then became very broad in subtropical Asia from the late Eocene (36 Ma) to the present. As documented in previous studies, the extreme Asian aridity evidenced from formations in the Junggar Basin of the Late Jurassic–Early Cretaceous (Jolivet et al., 2017) is well simulated from our results. Results from previous modelling studies show that central and western Asia was generally dry at the end of the Late Cretaceous, but was not identified as unvegetated dust provenance (Zhang et al., 2019). our results constrain the arid dust emission region to the central and west subtropical belt, which is also accordant to the proxy evidence of eolian dunes recorded in the earlier late Cretaceous (Farnsworth et al., 2019; Hasegawa et al., 2012). The permanent aridification recorded in the present-day Xining Basin originated from the late Eocene to Oligocene (40 Ma) (Licht et al., 2016; Bosboom et al., 2014), our simulations show the dust provenance appears since 36 Ma, which is in good agreement.

The dust emissions during the late Permian to the lower Jurassic are remarkably high over the whole Phanerozoic. Our results suggest that the extensive dust emissions across the tropical and subtropical supercontinent lasted from 265 Ma to 190 Ma. Flora biome evidence and a general lack of plant fossil record (Nowak et al., 2020) supports the massive desert environment which was distributed almost identically to our simulated dust provenance during the late Permian (256 Ma). Sediment records (Boucot et al., 2013) indicate similar massive aridity patterns as our simulations – the sediments reflecting wet and semi-arid environments in the central tropical land were not documented and the sediments reflecting arid environments were abundantly found along the edges of tropical and subtropical land since the Middle-Late Permian (265 Ma) to the middle Triassic (240 Ma) (Figure9), suggesting a massive extreme arid extended from subtropic to tropic during the corresponding times.

5.2 Implication and Limitation

Our study for the first time presents the dust emission variations over the past 540 Million years with the dust emission fields for each of the 109 corresponding time slices, which can serve as an archive both in the field of dust simulations and the paleoclimate. Similar simulations focusing on deep-time dust variations have been performed by Lin et al. (2024) with a different GCM and vegetation scheme. Our results in general support their conclusion that subtropical land is the major controlling factor in the dust variations since the late Permian, and extend this mechanism to the whole Phanerozoic with higher temporal resolution experiments. Further model-data comparison and model-model comparison can be carried out on this basis in the future to improve the understanding of deep-time dust variations and their mechanisms.

For the time periods where our results show high dust emissions, the radiation effect of dust is presumably very different from the pre-industrial time or the Last Glacial Maximum. The latter two are relatively well constrained, whereas the effects in high-emission paleo times are worth further diagnosis.

Some of the bias from our results may arise from details about the dust emission process that have to be omitted in this study. As mentioned in section 2.1, the particle size and topography parameters are significant to the physical dust emission

https://doi.org/10.5194/cp-2024-22
Preprint. Discussion started: 21 March 2024

process but are not included here due to a lack of information. Another aspect of bias is from the vegetation scheme used in our simulations. We here in this study assume plant functional types are consistent and the same as modern over the whole Phanerozoic, which will theoretically result in inappropriate vegetation outputs in the deep-time paleo. Our simulations after the Devonian (360 Ma) are supposed to be more robust than those prior to that when terrestrial flora was perhaps more similar to today. While this constant vegetation scheme is the common approach of most current paleoclimate modelling studies, the new trait-based whole-plant functional-strategy approach (Matthaeus et al., 2023) shows potential to be an alternative solution. Regarding the scope of this study is only looking at the non-vegetated area rather than a specific vegetation type, despite the unavoidable uncertainties coming with the vegetation scheme, We argue that the modelled dust and aridity are relatively robust, as any vegetation may have flourished where there was precipitation.

In this study, the dust emission model does not give a complete dust cycle, nor is it fully coupled to the GCM, so the dust feedback is not represented in the simulations. The effect of dust on the corresponding paleo climate could have been significant, especially for periods with enormous emissions. There have been many models do include the dust scheme (e.g. the CMIP6 models evaluated in (Zhao et al., 2022), and would take huge computational resources to run simulations of similar temporal resolution due to their complexity, while offline dust models are more suitable for carrying out multi-scale simulations with the defect of losing dynamic feedback between the dust cycle and the climate system.

6 Conclusions

In this study, we take advantage of a series of paleoclimate simulations carried out with the Earth System Model which cover 109 time slices over the whole Phanerozoic, and extend the experiments to dust emissions of the same resolutions with a newly developed dust emission model.

The dust emission model is first tuned to the modern and then applied to the paleo configurations. For the first time, Our study yields a time-series of global dust emission rates of the whole Phanerozoic, along with corresponding dust emission fields at the stage level resolution. Our results are evaluated by comparing them with sedimentary and plant fossil indicators. Model-data comparisons reveal that our simulations are in fair accordance with geological records.

The driving forces of dust emissions over time are analysed at different levels of mechanisms. From the perspective of dust emission-related surface processes, our results suggest the non-vegetated area is the predominant contributing factor to the multi-million-year-scale dust emissions variations, both in magnitude and in patterns of changes versus time. From the perspective of the geological timescale, our results suggest the CO_2 effect on dust emissions is negligible compared to the effect from paleogeography.

The key non-vegetated area driving factor draws the focus to the paleohydroclimate. Our results show the meridional precipitation patterns are rather stable throughout the Phanerozoic – more precipitation over the tropics and rare precipitation over the subtropics. Thus the mechanism of aridity area and dust emissions are explained by the continental land movement, the distance of land area to the closest sea in tropic and subtropic zones.

https://doi.org/10.5194/cp-2024-22
Preprint. Discussion started: 21 March 2024

Climate of the Past Discussions
Open Access
EGU

Code and data availability. The DUSTY model code is available from https://github.com/yixuan-coding/DUSTY_model. The simulated dust emissions fields are available from https://github.com/yixuan-coding/DUSTY_outputs

Appendix A: Appendix

Here we provide the detailed methods of factorisation used in section 4.2.

For the linear factorisation on l and b. The dust emissions contributed by l (ΔD^l) is calculated by:

$$\Delta D^l = D^l \tag{A1}$$

representing the dust emissions difference between the configuration in which there is no dust emission over the whole globe, and the configuration in which all the land area produces dust. The corresponding states of other variables in the configuration in which all land is vegetation-free are: $b = 1$, which means all the land surface is covered by 100% bare soil; $m = 0$, which means the surface soil is at its driest over all land; $s = 0$, which means there is no snow cover anywhere; $U = 1.91$ (in the choice of tuned parameter set version 1), indicating the surface wind speed that blows up the dust. Similarly, the dust emissions contributed by b (ΔD^b) is calculated by:

$$\Delta D^b = D^{lb} - D^l, \tag{A2}$$

which represents the difference in dust emission rate between the configuration in which all land is vegetation-free and the configuration in which dust sources are restricted to non-vegetated land areas. The corresponding states of other variables in this configuration are identical to those in the all land is vegetation-free configuration except that b is assigned specific values.

For the non-linear factorisation on d_m, d_s and d_U, the algorithm is as follows according to (Lunt et al., 2021) to calculate the difference between D and ΔD^{lb} :

The resulting equations for the factorisations are :

$$\begin{aligned}
\Delta D^m &= \frac{1}{6}\left[2(D^{lbm} - D^{lb}) + (D^{lbmU} - D^{lbU}) + (D^{lbms} - D^{lbs}) + 2(D^{lbmsU} - D^{lbsU})\right] \\
\Delta D^s &= \frac{1}{6}\left[2(D^{lbs} - D^{lb}) + (D^{lbms} - D^{lbm}) + (D^{lbsU} - D^{lbU}) + 2(D^{lbmsU} - D^{lbU})\right] \\
\Delta D^U &= \frac{1}{6}\left[2(D^{lbU} - D^{lb}) + (D^{lbmU} - D^{lbm}) + (D^{lbsU} - D^{lbs}) + 2(D^{lbmsU} - D^{lbms})\right]
\end{aligned} \tag{A3}$$

where the ΔD^m, ΔD^s and ΔD^U represent the difference in dust emission caused by the m, s and U from the "all-bare-land-dessert" configuration respectively.

The total dust emission rate is hence isolated as:

$$D = \Delta D^l + \Delta D^b + \Delta D^m + \Delta D^s + \Delta D^U \tag{A4}$$

https://doi.org/10.5194/cp-2024-22
Preprint. Discussion started: 21 March 2024

Climate of the Past Discussions
Open Access
EGU

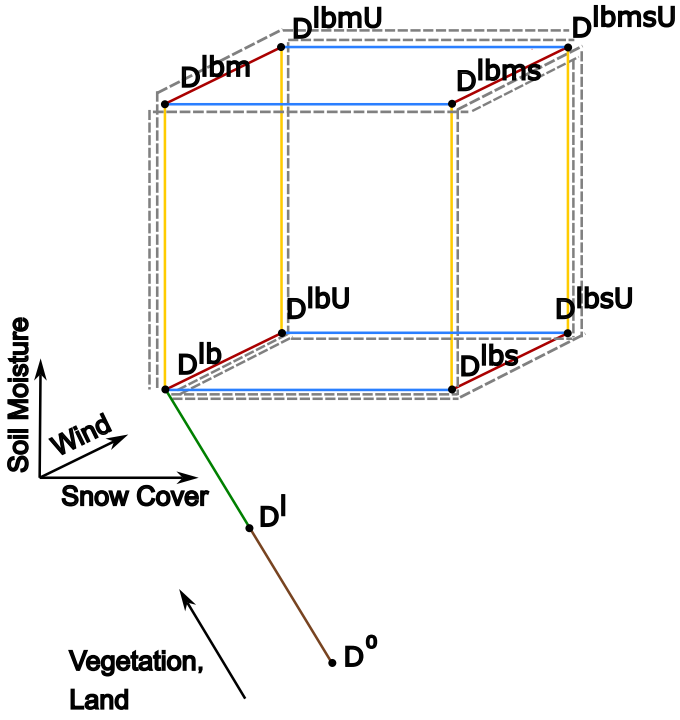

Figure A1. The factorisation method concept

https://doi.org/10.5194/cp-2024-22
Preprint. Discussion started: 21 March 2024

Climate of the Past
Discussions
Open Access
EGU

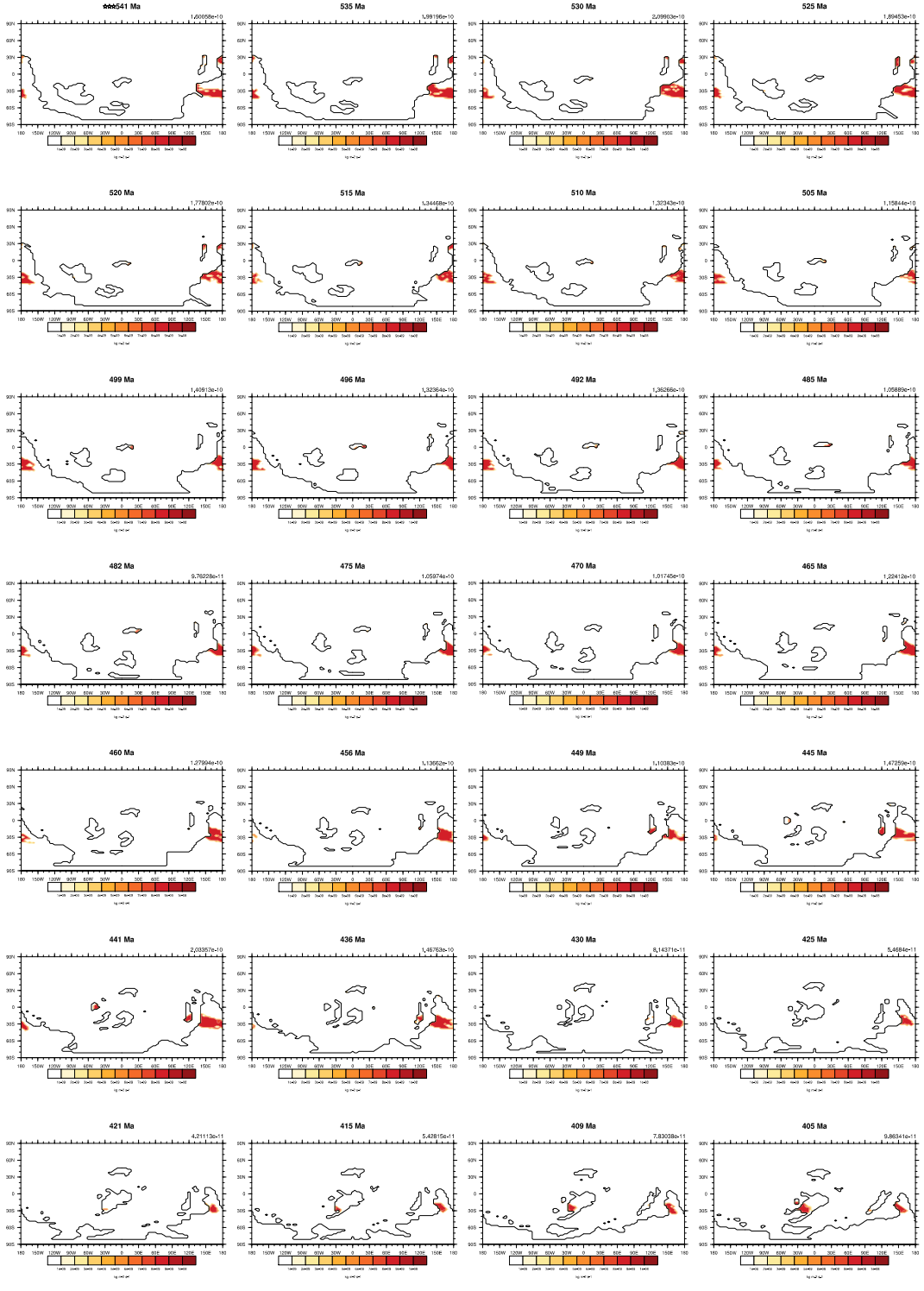

Figure A2. The simulated dust emissions of all 109 time slices over the Phanerozoic (Part 1). Values at the top-right are the global mean dust emission rates. Unites are $kg\ m^{-2}s^{-1}$.

https://doi.org/10.5194/cp-2024-22
Preprint. Discussion started: 21 March 2024

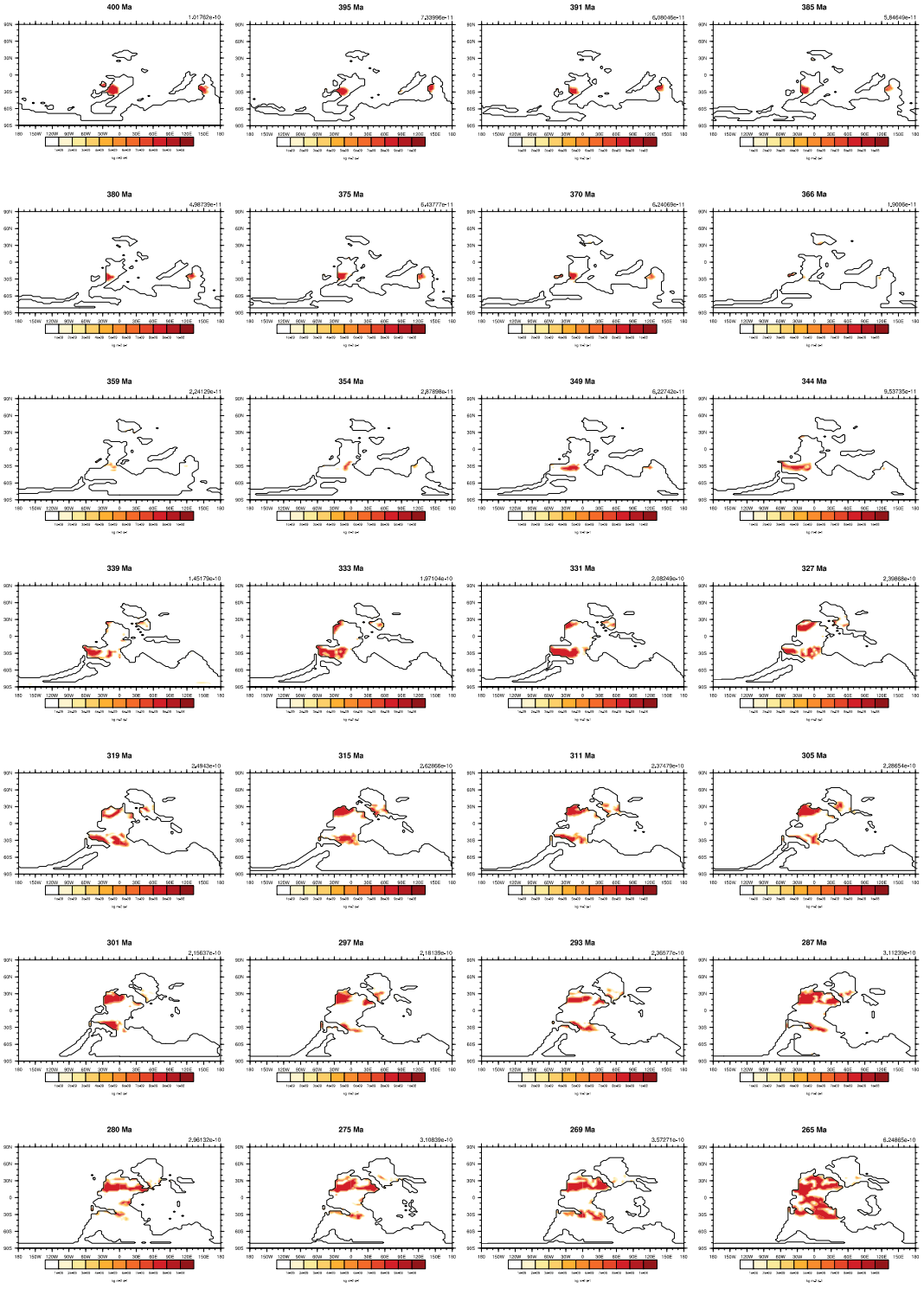

Figure A3. The simulated dust emissions of all 109 time slices over the Phanerozoic (Part 2). Values at the top-right are the global mean dust emission rates. Unites are $kg\ m^{-2}s^{-1}$.

https://doi.org/10.5194/cp-2024-22
Preprint. Discussion started: 21 March 2024

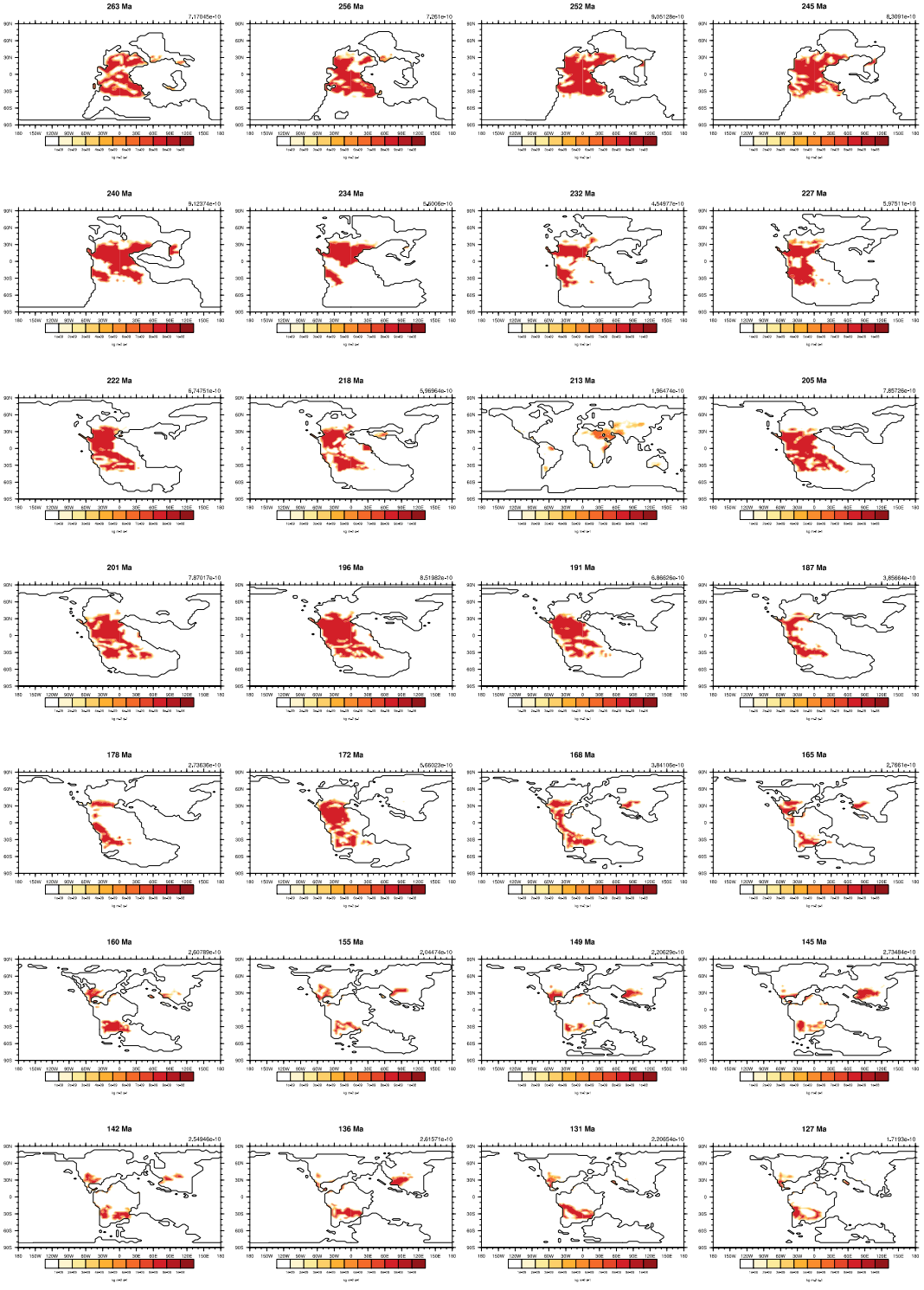

Figure A4. The simulated dust emissions of all 109 time slices over the Phanerozoic (Part 3). Values at the top-right are the global mean dust emission rates. Unites are $kg\ m^{-2}s^{-1}$.

https://doi.org/10.5194/cp-2024-22
Preprint. Discussion started: 21 March 2024

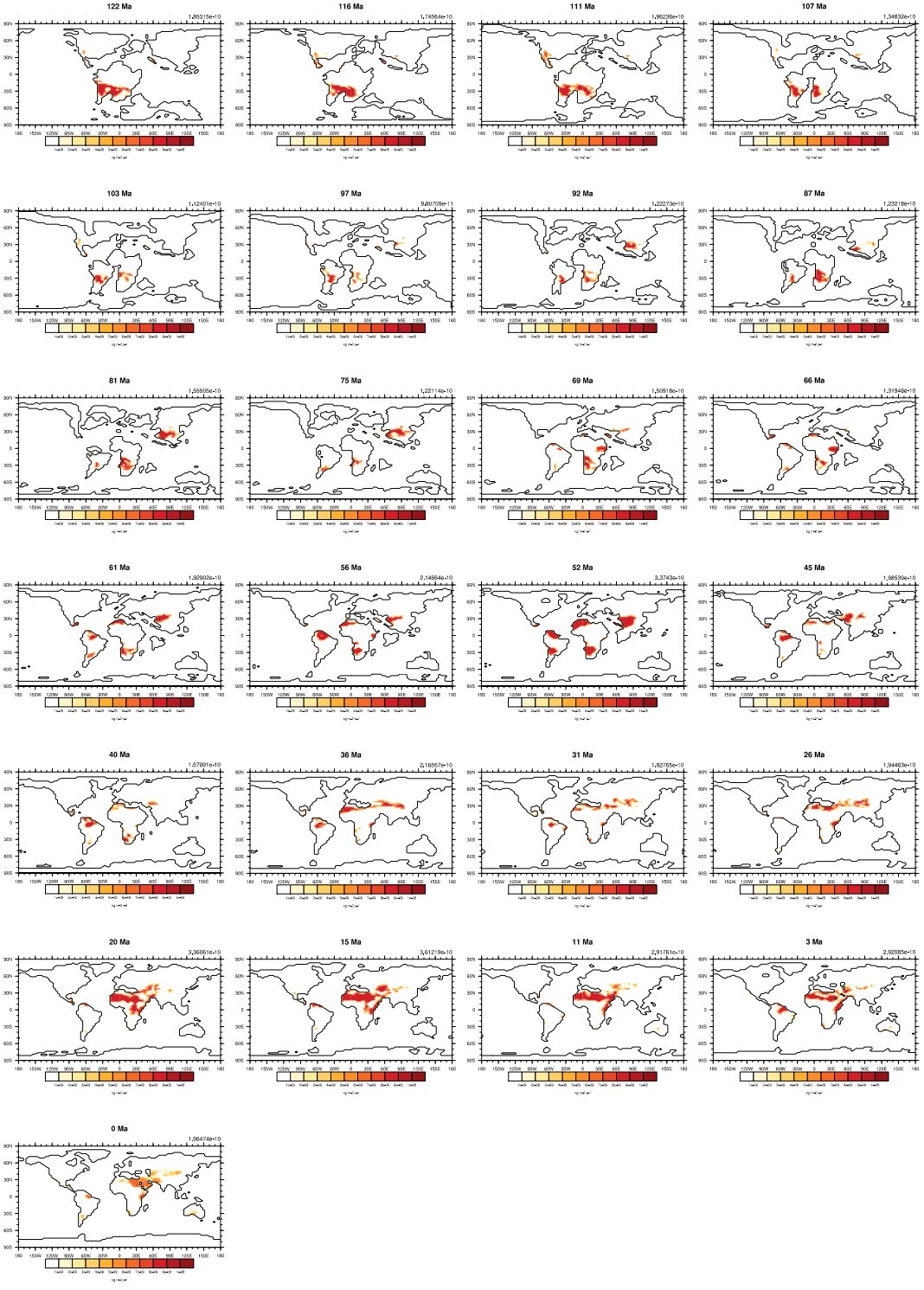

Figure A5. The simulated dust emissions of all 109 time slices over the Phanerozoic (Part 4). Values at the top-right are the global mean dust emission rates. Unites are $kg\ m^{-2}s^{-1}$.

https://doi.org/10.5194/cp-2024-22
Preprint. Discussion started: 21 March 2024

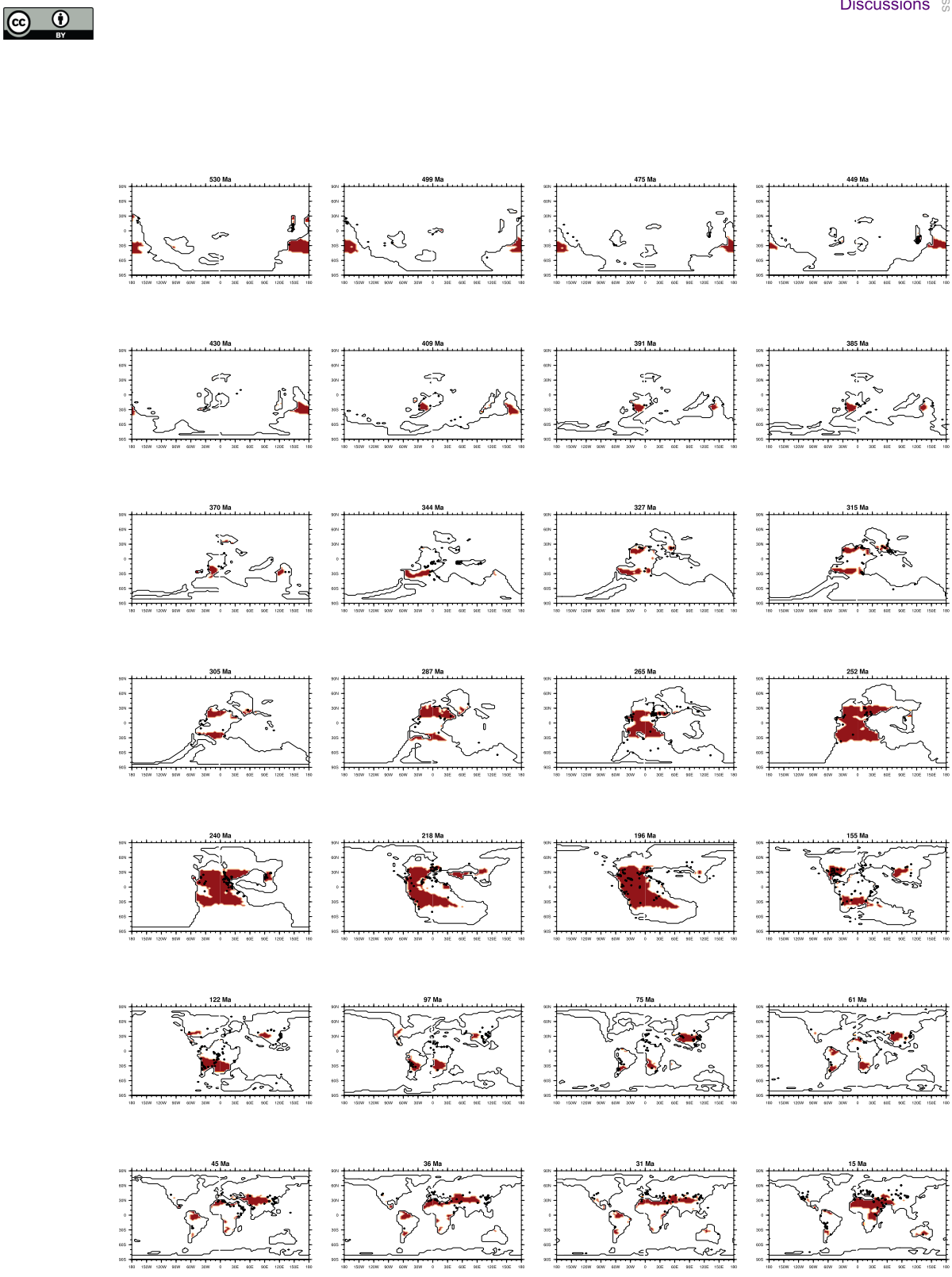

Figure A6. Comparisons of evaporite sedimentary records (dark dots, data from (Boucot et al., 2013)) to the simulated evaporite (area in red) of multiple time slices

https://doi.org/10.5194/cp-2024-22
Preprint. Discussion started: 21 March 2024

Climate of the Past Discussions

Author contributions. The study was developed by all authors. PJV performed the original HadCM3L model simulations. DJL and YX designed the study and developed the model code, wrote and edited the original manuscript.

Competing interests. The authors declare that they have no conflict of interest.

Acknowledgements. DJL and PJV acknowledge NERC grant NE/X000222/1 (PaleoGradPhan: Paleoclimate meridional and zonal Gradients in the Phanerozoic). YX acknowledges funding from the China Scholarship Council (Grant No. 202006380069).

https://doi.org/10.5194/cp-2024-22
Preprint. Discussion started: 21 March 2024

Climate of the Past Discussions

References

Anderson, C. H., Murray, R. W., Dunlea, A. G., Giosan, L., Kinsley, C. W., McGee, D., and Tada, R.: Aeolian delivery to Ulleung Basin, Korea (Japan Sea), during development of the East Asian Monsoon through the last 12 Ma, Geological Magazine, 157, 806–817, https://doi.org/10.1017/S001675681900013X, 2020.

Arakawa, A. and Lamb, V. R.: Computational Design of the Basic Dynamical Processes of the UCLA General Circulation Model, in: General Circulation Models of the Atmosphere, edited by CHANG, J., vol. 17 of *Methods in Computational Physics: Advances in Research and Applications*, pp. 173–265, Elsevier, https://doi.org/https://doi.org/10.1016/B978-0-12-460817-7.50009-4, 1977.

Bosboom, R. E., Abels, H. A., Hoorn, C., van den Berg, B. C., Guo, Z. J., and Dupont-Nivet, G.: Aridification in continental Asia after the Middle Eocene Climatic Optimum (MECO), Earth and Planetary Science Letters, 389, 34–42, https://doi.org/10.1016/j.epsl.2013.12.014, 2014.

Boucot, A. J., Xu, C., Scotese, C. R., and Morley, R. J.: Phanerozoic Paleoclimate: An Atlas of Lithologic Indicators of Climate, SEPM Concepts in Sedimentology and Paleontology, 11, ISBN 9781565762817, https://pubs.geoscienceworld.org/books/book/1966/, 2013.

Bullard, J. E., Baddock, M., Bradwell, T., Crusius, J., Darlington, E., Gaiero, D., Gassó, S., Gisladottir, G., Hodgkins, R., McCulloch, R., McKenna-Neuman, C., Mockford, T., Stewart, H., and Thorsteinsson, T.: High-latitude dust in the Earth system, https://doi.org/10.1002/2016RG000518, 2016.

Bushell, A.: Unified Model User Guide, chap. Clouds, p. 27, in: Matthews, https://gmd.copernicus.org/preprints/gmd-2017-16/gmd-2017-16.pdf, 1998.

Cakmur, R. V., Miller, R. L., Perlwitz, J., Geogdzhayev, I. V., Ginoux, P., Koch, D., Kohfeld, K. E., Tegen, I., and Zender, C. S.: Constraining the magnitude of the global dust cycle by minimizing the difference between a model and observations, 111, 1–24, https://doi.org/10.1029/2005JD005791, 2006.

Chen, S., Huang, J., Qian, Y., Zhao, C., Kang, L., Yang, B., Wang, Y., Liu, Y., Yuan, T., Wang, T., Ma, X., and Zhang, G.: An overview of mineral dust modeling over East Asia, Journal of Meteorological Research, 31, 633–653, https://doi.org/10.1007/s13351-017-6142-2, 2017.

Cox, M. D., Oceanic, G. F. D. L. N., and Administration), A.: A Primitive Equation, 3-dimensional Model of the Ocean, GFDL Ocean Group technical report, Geophysical Fluid Dynamica Laboratory/NOAA, Princeton University, https://books.google.co.uk/books?id=ayfaxwEACAAJ, 1984.

Cox, P., Betts, R., Bunton, C., Essery, R., Rowntree, P., and Smith, J.: The impact of new land surface physics on the GCM simulation of climate and climate sensitivity, Climate Dynamics, 15, 183–203, https://doi.org/10.1007/s003820050276, 1999.

DeCelles, P. G., Kapp, P., Ding, L., and Gehrels, G. E.: Late Cretaceous to middle Tertiary basin evolution in the central Tibetan Plateau: Changing environments in response to tectonic partitioning, aridification, and regional elevation gain, GSA Bulletin, 119, 654–680, https://doi.org/10.1130/B26074.1, 2007.

Diaz, H. F. and Bradley, R. S.: The Hadley circulation: Present, past, and future: An introduction, in: The Hadley circulation: present, past and future, pp. 1–5, Springer, 2004.

Edwards, J. M. and Slingo, A.: Studies with a flexible new radiation code. I: Choosing a configuration for a large-scale model, Quarterly Journal of the Royal Meteorological Society, 122, 689–719, https://doi.org/https://doi.org/10.1002/qj.49712253107, 1996.

https://doi.org/10.5194/cp-2024-22
Preprint. Discussion started: 21 March 2024

Farnsworth, A., Lunt, D. J., Robinson, S. A., Valdes, P. J., Roberts, W. H., Clift, P. D., Markwick, P., Su, T., Wrobel, N., Bragg, F., Kelland, S. J., and Pancost, R. D.: Past East Asian monsoon evolution controlled by paleogeography, not CO2, Tech. Rep. 10, ISSN 23752548, https://doi.org/10.1126/sciadv.aax1697, 2019.

Fitzsimmons, K. E., Cohen, T. J., Hesse, P. P., Jansen, J., Nanson, G. C., May, J. H., Barrows, T. T., Haberlah, D., Hilgers, A., Kelly, T., Larsen, J., Lomax, J., and Treble, P.: Late Quaternary palaeoenvironmental change in the Australian drylands, Quaternary Science Reviews, 74, 78–96, https://doi.org/10.1016/J.QUASCIREV.2012.09.007, 2013.

Foster, G. L., Royer, D. L., and Lunt, D. J.: Future climate forcing potentially without precedent in the last 420 million years, Nature Communications, 8, 1–8, https://doi.org/10.1038/ncomms14845, 2017.

Ginoux, P., Chin, M., Tegen, I., Goddard, T., and In, G.: Sources and distributions of dust aerosols simulated with the GOCART model, ournal of Geophysical Research, 106, 20 255–20 273, 2001.

Gkikas, A., Proestakis, E., Amiridis, V., Kazadzis, S., Di Tomaso, E., Tsekeri, A., Marinou, E., Hatzianastassiou, N., and Pérez Garciá-Pando, C.: ModIs Dust AeroSol (MIDAS): A global fine-resolution dust optical depth data set, Atmospheric Measurement Techniques, 14, 309–334, https://doi.org/10.5194/amt-14-309-2021, 2021.

Gough, D. O.: Solar interior structure and luminosity variations, Solar Physics, 74, 21–34, https://doi.org/10.1007/BF00151270, 1981.

Gregory, D., Kershaw, R., and Inness, P. M.: Parametrization of momentum transport by convection. II: Tests in single-column and general circulation models, Quarterly Journal of the Royal Meteorological Society, 123, 1153–1183, https://doi.org/https://doi.org/10.1002/qj.49712354103, 1997.

Hasegawa, H., Tada, R., Jiang, X., Suganuma, Y., Imsamut, S., Charusiri, P., Ichinnorov, N., and Khand, Y.: Drastic shrinking of the Hadley circulation during the mid-Cretaceous Supergreenhouse, Climate of the Past, 8, 1323–1337, https://doi.org/10.5194/cp-8-1323-2012, 2012.

Jickells, T. D., An, Z. S., Andersen, K. K., Baker, A. R., Bergametti, C., Brooks, N., Cao, J. J., Boyd, P. W., Duce, R. A., Hunter, K. A., Kawahata, H., Kubilay, N., LaRoche, J., Liss, P. S., Mahowald, N., Prospero, J. M., Ridgwell, A. J., Tegen, I., and Torres, R.: Global iron connections between desert dust, ocean biogeochemistry, and climate, Tech. Rep. 5718, ISSN 00368075, https://doi.org/10.1126/science.1105959, 2005.

Jolivet, M., Bourquin, S., Heilbronn, G., Robin, C., Barrier, L., Dabard, M. P., Jia, Y., De Pelsmaeker, E., and Fu, B.: The Upper Jurassic-Lower Cretaceous alluvial-fan deposits of the Kalaza Formation (Central Asia): Tectonic pulse or increased aridity?, Geological Society Special Publication, 427, 491–521, https://doi.org/10.1144/SP427.6, 2017.

Jones, L. A., Mannion, P. D., Farnsworth, A., Bragg, F., and Lunt, D. J.: Climatic and tectonic drivers shaped the tropical distribution of coral reefs, Nature Communications, 13, 1–10, https://doi.org/10.1038/s41467-022-30793-8, 2022.

Kerkweg, A., Sander, R., Tost, H., and Jöckel, P.: Technical note: Implementation of prescribed (OFFLEM), calculated (ONLEM), and pseudo-emissions (TNUDGE) of chemical species in the Modular Earth Submodel System (MESSy), Atmospheric Chemistry and Physics, 6, 3603–3609, https://doi.org/10.5194/acp-6-3603-2006, 2006.

Kiehl, J. T. and Shields, C. A.: Sensitivity of the palaeocene-eocene thermal maximum climate to cloud properties, Philosophical Transactions of the Royal Society A: Mathematical, Physical and Engineering Sciences, 371, https://doi.org/10.1098/rsta.2013.0093, 2013.

Kohfeld, K. E. and Harrison, S. P.: DIRTMAP: The geological record of dust, Earth-Science Reviews, 54, 81–114, https://doi.org/10.1016/S0012-8252(01)00042-3, 2001.

Kok, J. F., Parteli, E. J., Michaels, T. I., Karam, D. B., R Parteli, E. J., Michaels, T. I., Bou Karam, D., F, K. J., J R, P. E., I, M. T., and Karam, B. D.: The physics of wind-blown sand and dust, vol. 75, https://doi.org/10.1088/0034-4885/75/10/106901, 2012.

https://doi.org/10.5194/cp-2024-22
Preprint. Discussion started: 21 March 2024

Kok, J. F., Mahowald, N. M., Fratini, G., Gillies, J. A., Ishizuka, M., Leys, J. F., Mikami, M., Park, M. S., Park, S. U., Van Pelt, R. S., and Zobeck, T. M.: An improved dust emission model - Part 1: Model description and comparison against measurements, Atmospheric Chemistry and Physics, 14, 13 023–13 041, https://doi.org/10.5194/acp-14-13023-2014, 2014.

Lamy, F., Gersonde, R., Winckler, G., Esper, O., Jaeschke, A., Kuhn, G., Ullermann, J., Martínez-Garcia, A., Lambert, F., and Kilian, R.: Increased dust deposition in the Pacific Southern Ocean during glacial periods, Science, 343, 403–407, 2014.

Licht, A., Dupont-Nivet, G., Pullen, A., Kapp, P., Abels, H. A., Lai, Z., Guo, Z., Abell, J., and Giesler, D.: Resilience of the Asian atmospheric circulation shown by Paleogene dust provenance, Nature Communications, 7, https://doi.org/10.1038/ncomms12390, 2016.

Lin, Q., Liu, Y., Guo, J., Li, X., Lan, J., Zuo, H., Zhang, M., Zhang, J., Zhao, Z., Yuan, S., Bao, X., and Hu, Y.: Simulated dust activity in typical time periods of the past 250 million years, Fundamental Research, https://doi.org/10.1016/j.fmre.2024.02.004, 2024.

Liu, P., Liu, Y., Peng, Y., Lamarque, J. F., Wang, M., and Hu, Y.: Large influence of dust on the Precambrian climate, Nature Communications, 11, 1–8, https://doi.org/10.1038/s41467-020-18258-2, 2020.

Lunt, D. J. and Valdes, P. J.: The modern dust cycle: Comparison of model results with observations and study of sensitivities, Journal of Geophysical Research Atmospheres, 107, 1–1, https://doi.org/10.1029/2002JD002316, 2002.

Lunt, D. J., Chandan, D., Haywood, A. M., Lunt, G. M., Rougier, J. C., Salzmann, U., Schmidt, G. A., and Valdes, P. J.: Multi-variate factorisation of numerical simulations, Geoscientific Model Development, 14, 4307–4317, https://doi.org/10.5194/gmd-14-4307-2021, 2021.

Mahowald, N. M., Scanza, R., Brahney, J., Goodale, C. L., Hess, P. G., Moore, J. K., and Neff, J.: Aerosol Deposition Impacts on Land and Ocean Carbon Cycles, Current Climate Change Reports, 3, 16–31, https://doi.org/10.1007/s40641-017-0056-z, 2017.

Marx, S. K., Kamber, B. S., McGowan, H. A., Petherick, L. M., McTainsh, G. H., Stromsoe, N., Hooper, J. N., and May, J. H.: Palaeo-dust records: A window to understanding past environments, Global and Planetary Change, 165, 13–43, https://doi.org/10.1016/j.gloplacha.2018.03.001, 2018.

Marzocchi, A., Lunt, D. J., Flecker, R., Bradshaw, C. D., Farnsworth, A., and Hilgen, F. J.: Orbital control on late Miocene climate and the North African monsoon: insight from an ensemble of sub-precessional simulations, Climate of the Past, 11, 1271–1295, https://doi.org/10.5194/cp-11-1271-2015, 2015.

Matthaeus, W. J., Macarewich, S. I., Richey, J., Montañez, I. P., Mcelwain, J. C., White, J. D., Wilson, J. P., and Poulsen, C. J.: A Systems Approach to Understanding How Plants Transformed Earth's Environment in Deep Time, Annual Review of Earth and Planetary Sciences, 51, 551–580, https://doi.org/10.1146/annurev-earth-080222-082017, 2023.

Mckay, M., Beckman, R., and Conover, W.: A Comparison of Three Methods for Selecting Vales of Input Variables in the Analysis of Output From a Computer Code, Technometrics, 21, 239–245, https://doi.org/10.1080/00401706.1979.10489755, 1979.

Miller, R. L., Cakmur, R. V., Perlwitz, J., Geogdzhayev, I. V., Ginoux, P., Koch, D., Kohfeld, K. E., Prigent, C., Ruedy, R., Schmidt, G. A., and Tegen, I.: Mineral dust aerosols in the NASA Goddard Institute for Space Sciences ModelE atmospheric general circulation model, Journal of Geophysical Research Atmospheres, 111, 1–19, https://doi.org/10.1029/2005JD005796, 2006.

Muhs, D. R.: The geologic records of dust in the quaternary, Aeolian Research, 9, 3–48, https://doi.org/10.1016/j.aeolia.2012.08.001, 2013.

Nguyen, H., Evans, A., Lucas, C., Smith, I., and Timbal, B.: The Hadley Circulation in Reanalyses: Climatology, Variability, and Change, Journal of Climate, 26, 3357–3376, https://doi.org/https://doi.org/10.1175/JCLI-D-12-00224.1, 2013.

Niedermeyer, E. M., Schefuß, E., Sessions, A. L., Mulitza, S., Mollenhauer, G., Schulz, M., and Wefer, G.: Orbital- and millennial-scale changes in the hydrologic cycle and vegetation in the western African Sahel: insights from individual plant wax δD and δ13C, Quaternary Science Reviews, 29, 2996–3005, https://doi.org/10.1016/J.QUASCIREV.2010.06.039, 2010.

https://doi.org/10.5194/cp-2024-22
Preprint. Discussion started: 21 March 2024

Nowak, H., Vérard, C., and Kustatscher, E.: Palaeophytogeographical Patterns Across the Permian–Triassic Boundary, Frontiers in Earth Science, 8, 1–16, https://doi.org/10.3389/feart.2020.613350, 2020.

Pérez, C., Haustein, K., Janjic, Z., Jorba, O., Huneeus, N., Baldasano, J. M., Black, T., Basart, S., Nickovic, S., Miller, R. L., Perlwitz, J. P., Schulz, M., and Thomson, M.: Atmospheric dust modeling from meso to global scales with the online NMMB/BSC-Dust model – Part 1: Model description, annual simulations and evaluation, Atmospheric Chemistry and Physics, 11, 13 001–13 027, https://doi.org/10.5194/acp-11-13001-2011, 2011.

Rea, D. K., Snoeckx, I., and Joseph, L. H.: Late Cenozoic Eolian deposition in the North Pacific: Asian drying, Tibetan uplift, and cooling of the northern hemisphere, Paleoceanography, 13, 215–224, https://doi.org/10.1029/98PA00123, 1998.

Ross, P.: Deep ocean circulation during the early Eocene: A model-data comparison., Ph.D. thesis, Imperial College London, 2023.

Sagoo, N., Valdes, P., Flecker, R., and Gregoire, L. J.: The early eocene equable climate problem: Can perturbations of climate model parameters identify possible solutions?, Philosophical Transactions of the Royal Society A: Mathematical, Physical and Engineering Sciences, 371, https://doi.org/10.1098/rsta.2013.0123, 2013.

Schepanski, K.: Transport of mineral dust and its impact on climate, Geosciences, 8, https://doi.org/10.3390/geosciences8050151, 2018.

Scotese, C. R.: PALEOMAP PaleoAtlas for GPlates and the PaleoData plotter program, PALEOMAP project, 2016.

Scotese, C. R. and Wright, N. M.: PALEOMAP Paleodigital Elevation Models (PaleoDEMS) for the Phanerozoic by Christopher R . Scotese and Nicky Wright Research School of Earth Sciences , Australian National University, pp. 1–26, https://www.earthbyte.org/paleodem-resource-scotese-and-wright-2018/, 2018.

Shao, Y.: A model for mineral dust emission, Journal of Geophysical Research Atmospheres, 106, 20 239–20 254, https://doi.org/10.1029/2001JD900171, 2001.

Tegen, I. and Fung, I.: Modeling of mineral dust in the atmosphere: sources, transport, and optical thickness, Journal of Geophysical Research, 99, 1994.

Turner, J. S. and Kraus, E. B.: A one-dimensional model of the seasonal thermocline I. A laboratory experiment and its interpretation, Tellus, 19, 88–97, https://doi.org/10.3402/tellusa.v19i1.9752, 1967.

Valdes, P. J., Armstrong, E., Badger, M. P., Bradshaw, C. D., Bragg, F., Crucifix, M., Davies-Barnard, T., Day, J., Farnsworth, A., Gordon, C., Hopcroft, P. O., Kennedy, A. T., Lord, N. S., Lunt, D. J., Marzocchi, A., Parry, L. M., Pope, V., Roberts, W. H., Stone, E. J., Tourte, G. J., and Williams, J. H.: The BRIDGE HadCM3 family of climate models: HadCM3@Bristol v1.0, Geoscientific Model Development, 10, 3715–3743, https://doi.org/10.5194/gmd-10-3715-2017, 2017.

Valdes, P. J., Scotese, C. R., and Lunt, D. J.: Deep ocean temperatures through time, Climate of the Past, 17, 1483–1506, https://doi.org/10.5194/cp-17-1483-2021, 2021.

Vallé, F., Westerhold, T., and Dupont, L. M.: Orbital-driven environmental changes recorded at ODP Site 959 (eastern equatorial Atlantic) from the Late Miocene to the Early Pleistocene, International Journal of Earth Sciences, 106, 1161–1174, https://doi.org/10.1007/s00531-016-1350-z, 2017.

Wade, D. C., Luke Abraham, N., Farnsworth, A., Valdes, P. J., Bragg, F., and Archibald, A. T.: Simulating the climate response to atmospheric oxygen variability in the Phanerozoic: A focus on the Holocene, Cretaceous and Permian, Climate of the Past, 15, 1463–1483, https://doi.org/10.5194/cp-15-1463-2019, 2019.

Wang, F., Li, Z., Sun, X., Zhao, J., Fan, Y., Xia, D., Ayyamperumal, R., and Li, B.: Early Cretaceous (late Barremian - Early Albian) expanding aeolian activity in East Asia: Evidence from the stratigraphic evolution of aeolian deposition in the Baiyin-Jingyuan Basin, northern China, GSA Bulletin, pp. 1–26, https://doi.org/10.1130/b36747.1, 2023.

https://doi.org/10.5194/cp-2024-22
Preprint. Discussion started: 21 March 2024

Watterson, I. G., Bathols, J., and Heady, C. B. T. B. o. t. A. M. S.: What influences the skill of climate models over the continents? Simple skill scores for CMIP5 and CMIP3 climate models are analyzed for each continent and the globe, 95, 689+, https://link.gale.com/apps/doc/A376683387/AONE?u=anon~2463951d&sid=googleScholar&xid=e8a28062, 2014.

White, A. A. and Bromley, R. A.: Dynamically consistent, quasi-hydrostatic equations for global models with a complete representation of the Coriolis force, Quarterly Journal of the Royal Meteorological Society, 121, 399–418, https://doi.org/https://doi.org/10.1002/qj.49712152208, 1995.

Wilson, D.: Unified Model User Guide, chap. Precipitation, p. 32, in: Matthews, https://ukscience.org/_Media/UM_User_Guide.pdf, 1998.

Winckler, G., Anderson, R. F., Fleisher, M. Q., McGee, D., and Mahowald, N.: Covariant glacial-interglacial dust fluxes in the equatorial Pacific and Antarctica, Science, 320, 93–96, https://doi.org/10.1126/science.1150595, 2008.

Yang, Y., Galy, A., Fang, X., Yang, R., Zhang, W., Song, B., Liu, Y., Han, W., Zhang, W., and Yang, S.: Neodymium isotopic constraints on Cenozoic Asian dust provenance changes linked to the exhumation history of the northern Tibetan Plateau and the Central Asian Orogenic Belt, Geochimica et Cosmochimica Acta, 296, 38–55, https://doi.org/10.1016/j.gca.2020.12.026, 2021.

Zender, C. S., Newman, D., and Torres, O.: Spatial heterogeneity in aeolian erodibility : Uniform , topographic , geomorphic , and hydrologic hypotheses, 108, https://doi.org/10.1029/2002JD003039, 2003.

Zhang, J., Liu, Y., Fang, X., Wang, C., and Yang, Y.: Large dry-humid fluctuations in Asia during the Late Cretaceous due to orbital forcing: A modeling study, Palaeogeography, Palaeoclimatology, Palaeoecology, 533, 109 230, https://doi.org/10.1016/j.palaeo.2019.06.003, 2019.

Zhang, W., Chen, J., Ji, J., and Li, G.: Evolving flux of Asian dust in the North Pacific Ocean since the late Oligocene, Aeolian Research, 23, 11–20, https://doi.org/10.1016/j.aeolia.2016.09.004, 2016.

Zhao, A., Ryder, C. L., and Wilcox, L. J.: How well do the CMIP6 models simulate dust aerosols?, Atmospheric Chemistry and Physics Discussions, 22, 1–32, https://doi.org/10.5194/acp-22-2095-2022, 2022.

Zhu, Z., Kuang, H., Liu, Y., Benton, M. J., Newell, A. J., Xu, H., An, W., Ji, S., Xu, S., Peng, N., and Zhai, Q.: Intensifying aeolian activity following the end-Permian mass extinction: Evidence from the Late Permian–Early Triassic terrestrial sedimentary record of the Ordos Basin, North China, Sedimentology, 67, 2691–2720, https://doi.org/10.1111/sed.12716, 2020.